A Z_{DR} Column Detection Algorithm to Examine Convective Storm Updrafts

JEFFREY C. SNYDER AND ALEXANDER V. RYZHKOV

Cooperative Institute for Mesoscale Meteorological Studies, University of Oklahoma, and NOAA/OAR/National Severe Storms Laboratory, Norman, Oklahoma

MATTHEW R. KUMJIAN

Department of Meteorology, The Pennsylvania State University, University Park, Pennsylvania

ALEXANDER P. KHAIN

Department of Atmospheric Sciences, Hebrew University of Jerusalem, Jerusalem, Israel

JOSEPH PICCA

NOAA/NWS/NCEP/Storm Prediction Center, Norman, Oklahoma

(Manuscript received 21 May 2015, in final form 15 September 2015)

ABSTRACT

Observations and recent high-resolution numerical model simulations indicate that liquid water and partially frozen hydrometeors can be lofted considerably above the environmental 0°C level in the updrafts of convective storms owing to the warm thermal perturbation from latent heating within the updraft and to the noninstantaneous nature of drop freezing. Consequently, upward extensions of positive differential reflectivity (i.e., $Z_{DR} \geq 1$ dB)—called Z_{DR} columns—may be a useful proxy for detecting the initiation of new convective storms and examining the evolution of convective storm updrafts. High-resolution numerical simulations with spectral bin microphysics and a polarimetric forward operator reveal a strong spatial association between updrafts and Z_{DR} columns and show the utility of examining the structure and evolution of Z_{DR} columns for assessing updraft evolution. This paper introduces an automated Z_{DR} column algorithm designed to provide additional diagnostic and prognostic information pertinent to convective storm nowcasting. Although suboptimal vertical resolution above the 0°C level and limitations imposed by commonly used scanning strategies in the operational WSR-88D network can complicate Z_{DR} column detection, examples provided herein show that the algorithm can provide operational and research-focused meteorologists with valuable information about the evolution of convective storms.

1. Introduction

The information provided by the transmission and reception of orthogonally polarized microwaves from polarimetric weather radar has led to appreciable gains in the understanding of precipitation distributions and microphysical processes that occur within deep moist convective storms. For example, the location of the melting layer within stratiform precipitation has a well-defined signature that is often easily identified in polarimetric radar data (e.g., Zrnić et al. 1993; Brandes and Ikeda 2004; Giangrande et al. 2008). Another important polarimetric signature is the appearance of an upward extension of enhanced differential reflectivity Z_{DR} above the ambient 0°C level near and within convective storm updrafts (e.g., Illingworth et al. 1987; Caylor and Illingworth 1987; Wakimoto and Bringi 1988; Bringi et al. 1991; Conway and Zrnić 1993; Brandes et al. 1995; Jameson et al. 1996; Hubbert et al. 1998; Smith et al. 1999; Kennedy et al. 2001; Loney et al. 2002; Kumjian and Ryzhkov 2008; Snyder et al. 2013). The reader is referred to Kumjian et al. (2014) for a more thorough review of previous Z_{DR} column observations and to Doviak and Zrnić (1993), Bringi and Chandrasekar (2001), and Kumjian (2013a,b,c) for a

Corresponding author address: Jeffrey Snyder, National Severe Storms Laboratory–RRDD, 120 David L. Boren Blvd., Norman, OK 73072.
E-mail: jeffrey.snyder@noaa.gov

discussion of commonly used polarimetric radar quantities, including radar reflectivity factor at horizontal polarization Z_H, differential reflectivity factor, copolar cross-correlation coefficient at lag 0 ρ_{hv}, differential phase Φ_{DP}, and specific differential phase K_{DP}.

Of most relevance for this paper, Z_{DR} (Seliga and Bringi 1976) tends to be proportional to the aspect ratio of hydrometeors that are small compared the radar's wavelength along the linear, orthogonal polarization planes used by the radar (e.g., typically horizontal H and vertical V) and with increasing dielectric constant. For example, Z_{DR} of raindrops tends to be near 0 dB for small drops and increases to ~5 dB (at S and X bands) or ~7 dB (at C band) for the larger, more oblate drops (e.g., ~8 mm in equivalent spherical diameter). Although hail can come in a wide variety of shapes (e.g., Browning 1966; Knight and Knight 1970a,b), it tends to be characterized by Z_{DR} near 0 dB owing to the quasi-isotropic scattering behavior as it tumbles, but it can be slightly negative if prolate or electromagnetically large and oblate (for which resonance effects can be significant). If a water coating develops on its surface, such as occurs during melting or wet growth, Z_{DR} may exceed 3 dB (e.g., Ryzhkov et al. 2013). Straka et al. (2000), Park et al. (2009), and Kumjian (2013a) provide more details on the Z_{DR} characteristics of different types of hydrometeors.

Within the updrafts of convective storms, the local 0°C level is perturbed upward owing to vertical advection and the latent heating effects of condensation (and, to a lesser extent, of fusion) within a positively buoyant updraft. Consequently, liquid precipitation within the updraft can be lofted well above the environmental 0°C level. More important from the perspective of precipitation microphysics, liquid raindrops do not freeze instantly upon entering a subfreezing environment; there is a nontrivial delay as raindrop freezing occurs (e.g., Bigg 1953; Johnson and Hallett 1968; Pruppacher and Klett 1997; Smith et al. 1999; Kumjian et al. 2012). For example, depending upon temperature and size, it may take several minutes for a raindrop to freeze completely. Smaller drops tend to freeze more quickly but begin freezing at lower temperatures than do larger drops, and freezing occurs more rapidly as the temperature decreases (e.g., Pruppacher and Klett 1997).

Because raindrops can produce Z_{DR} exceeding a few decibels, the lofting of drops above the 0°C level can produce Z_{DR} of similar magnitudes. Depending upon the sizes of the drops and the presence of other hydrometeors, relatively high Z_{DR} can extend several kilometers above the 0°C level in what is termed the Z_{DR} column.

In situ observations of aircraft transects through Z_{DR} columns reported in Bringi et al. (1991, 1996), Brandes et al. (1995), Smith et al. (1999), and Loney et al. (2002) showed Z_{DR} columns to be nearly collocated with the updraft and composed of substantial amounts of supercooled liquid water. Other observational studies, such as the dual-Doppler analyses presented in Kennedy et al. (2001), support the close spatial association between the updraft and the Z_{DR} column. Numerical modeling results (e.g., Kumjian et al. 2012, 2014; Snyder 2013) have shown not only that Z_{DR} columns tend to be nearly collocated with updrafts but also that the depth of Z_{DR} columns tends to be proportional to updraft intensity.

Detecting and warning for severe convective storms is a very important task for operational meteorologists. Anticipating and understanding the evolution of such storms can have important ramifications on warning lead time and performance. To have a good grasp of short-term convective storm threats and trends, it is often useful to have an understanding of the intensity of convective storm updrafts (e.g., see NOAA/NWS/ Warning Decision Training Division 2015). For example, increasing updraft intensity can be associated with an increase in low-level vertical vorticity (via increased stretching of vertical vorticity) and with increasing mass flux that may be relevant for the production of hail, heavy rain, and lightning; updraft intensification may have direct relevance for severe weather warning decisions. Unfortunately, the detection and quantification of convective storm updrafts observed by conventional, single-polarization radar can be difficult owing to the fact that scatterers that contribute to Z_H can be located far from updrafts. The bounded weak-echo region (BWER; Chisholm 1973), sometimes called the vault (Browning and Donaldson 1963), has been used to identify and provide some information on the intensity of updrafts. A BWER is characterized by a (typically quasi-circular or quasi-elliptical) ring of enhanced Z_H surrounding a local minimum in Z_H; if the enhanced Z_H does not completely enclose the region of reduced Z_H, it is typically called the weak-echo region (WER).

Owing to the dangers of collecting observations near BWERs, there are a limited number of in situ observations of WERs and BWERs. Musil et al. (1976) examined data from an armored aircraft penetrating an intense convective storm and found the WER to be characterized by very strong upward velocities exceeding 50 m s^{-1} and very little precipitation. Using dual-Doppler analysis, Calhoun et al. (2013), among others, noted a strong association between the locations of a BWER and the primary updraft of a supercell. Therefore, one may expect there to be an association between Z_{DR} columns and BWERs since both are associated
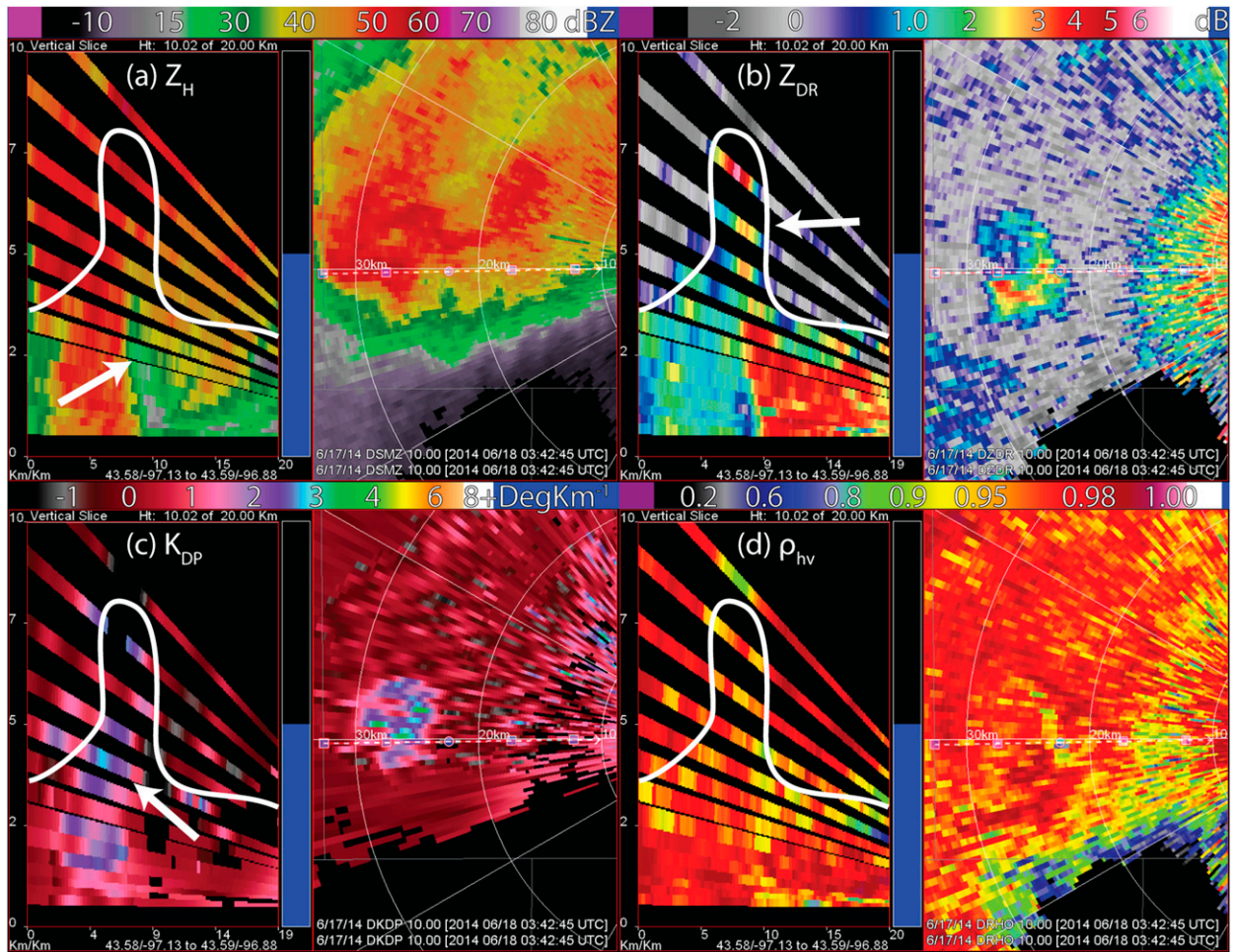
FIG. 1. Reconstructed (left) RHIs and (right) PPIs at 10.0° elevation angle showing (a) Z_H (dBZ), (b) Z_{DR} (dB), (c) K_{DP} (° km^{-1}), and (d) ρ_{hv} from the WSR-88D in Sioux Falls, South Dakota (KFSD), on the evening of 17 Jun 2014. The white arrows mark the BWER, Z_{DR} column, and K_{DP} column in (a),(b), and (c), respectively. The approximate edge of $Z_{DR} \geq 1$ dB is shown as a white curve in the reconstructed RHIs. To improve clarity and reduce noise, data shown are those output from the WSR-88D preprocessor, which means that the data presented are range filtered by averaging over a three- (for Z_H) and five-gate (for Z_{DR} and ρ_{hv}) sliding window centered on a given range gate.

with the updrafts of convective storms. In the supercell cases examined for this paper, such an association indeed exists, although it is quite common to see a Z_{DR} column in the absence of a BWER. For example, on 17 June 2014, a strong supercell in southeastern South Dakota was associated with a BWER evident up to ~5 km AGL (white arrow in Fig. 1a) and a Z_{DR} column that extended up to at least 7 km AGL (white arrow in Fig. 1b). An area of Z_{DR} near −1 dB was located atop the Z_{DR} column. A K_{DP} column, although not the subject of this paper, can be seen as an upward extension of enhanced K_{DP} (white arrow in Fig. 1c) that also extends to ~7 km AGL. A minor reduction in ρ_{hv} is seen in the Z_{DR} column (with $\rho_{hv} \sim 0.97$–0.99), whereas an appreciable reduction is seen immediately above the Z_{DR} column (where ρ_{hv} decreases to ~0.82), consistent with

other observations of reduced ρ_{hv} or enhanced linear depolarization ratio (LDR) near the top of the Z_{DR} columns (e.g., Bringi et al. 1997; Hubbert et al. 1998; Picca and Ryzhkov 2012; Snyder et al. 2013, 2014; Kumjian et al. 2014).

Another example of a prominent BWER comes from a tornadic supercell in central Oklahoma on 19 May 2013 (Fig. 2). A prominent Z_{DR} column is nearly collocated with the BWER; the BWER extends to nearly 8 km AGL, whereas the Z_{DR} column extends to ~6.3 km AGL. Since the BWER can be characterized as a minimum within a local maximum (i.e., the convective storm) in reflectivity factor, it is not particularly easy to design an algorithm to diagnose this feature, although Lakshmanan and Witt (1997) describe such an algorithm. In addition, merging convective storms or
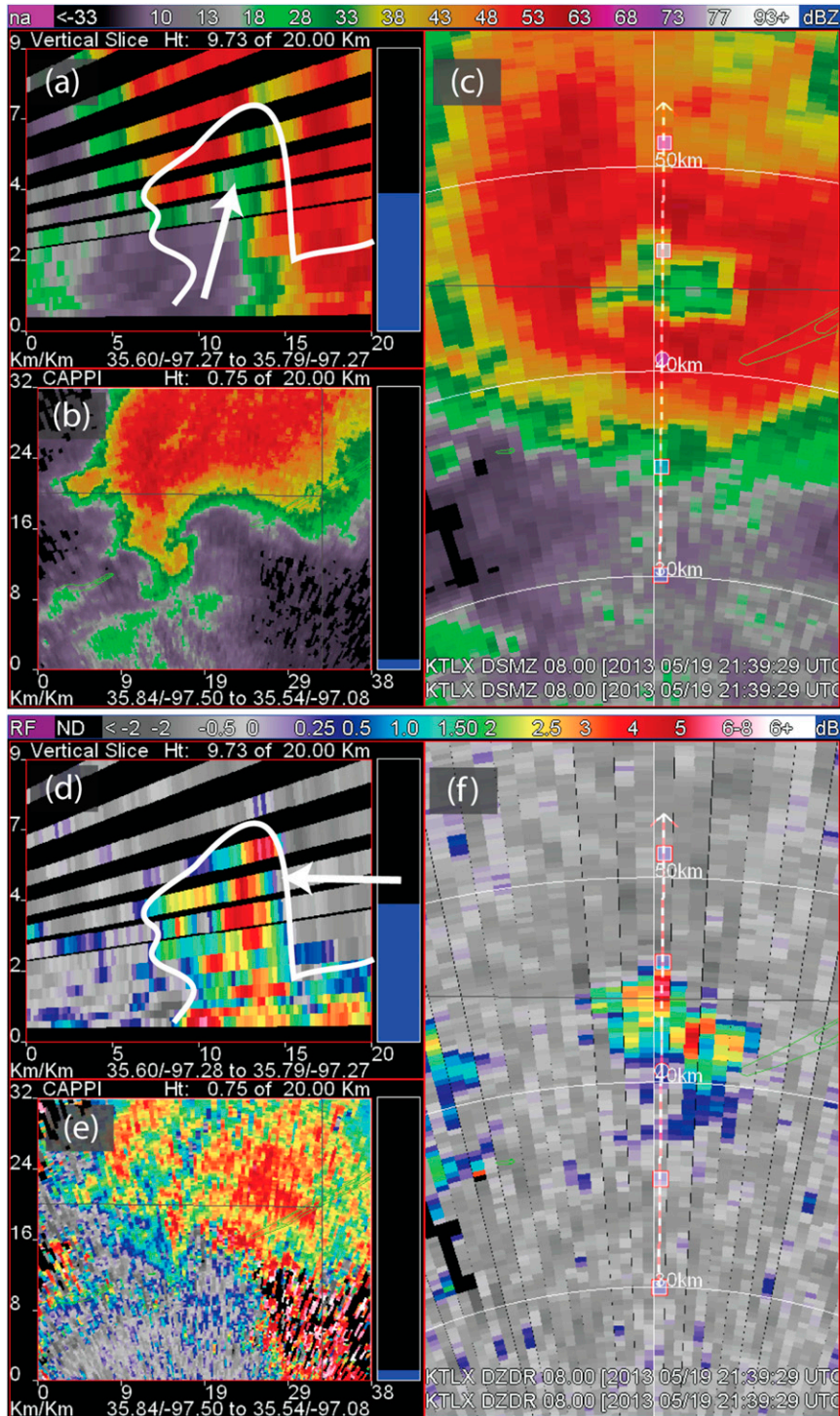
FIG. 2. Plots of (top) Z_H (dBZ) and (bottom) Z_{DR} (dB) from KTLX at 2139 UTC 19 May 2013 as (a),(d) reconstructed RHIs; (b),(e) constant altitude PPIs (i.e., CAPPIs) at ~750 m above radar level; and (c),(f) 8.0° elevation angle PPIs. The white arrow in (a) highlights the deep BWER; the white arrow in (d) highlights the Z_{DR} column. The approximate edge of $Z_{DR} \geq 1$ dB is shown as a white curve in (a) and (d). As in Fig. 1, data shown are those from the WSR-88D preprocessor; Z_H and Z_{DR} have been filtered through centered three- and five-gate averaging filters, respectively.

other processes can create local minima in Z_H that are not associated with BWERs (at least how the term BWER is typically used). In contrast, Z_{DR} columns represent local maxima in the Z_{DR} field and may be the only substantial, vertically continuous areas of high Z_{DR} above the 0°C height within and near convective storms; thus, they may be more conducive to automated detection.

The purpose of this paper is to describe a Z_{DR} column identification algorithm being developed at the National Severe Storms Laboratory (NSSL) and to show how this algorithm may provide useful information to operational meteorologists. Section 2 of this paper examines Z_{DR} columns produced by a high-resolution numerical model with spectral bin microphysics and a radar forward operator. Section 3 describes the algorithm and discusses some of the problems faced when quantifying Z_{DR} column characteristics using operational radar data. Section 4 presents several examples of Z_{DR} column algorithm output for examining convective storm initiation and evolution in supercells and other convective storm types. Some concluding remarks regarding the algorithm and a subjective assessment of Z_{DR} columns are provided in section 5.

2. Simulating Z_{DR} columns

Because in situ data collection of hydrometeor distributions within the updrafts of severe convective storms can be dangerous, only a few cases with such observations of hydrometeor types, sizes, and concentrations near Z_{DR} columns are present in the literature (e.g., Bringi et al. 1991, 1996; Brandes et al. 1995; Smith et al. 1999; Loney et al. 2002). As is often done when one wants to examine difficult-to-measure phenomena, we will turn to numerical modeling to help elucidate what is happening within the updrafts of severe convective storms and Z_{DR} columns.

Polarimetric signatures associated with numerically simulated convective storms have recently been examined following the development of polarimetric emulators (e.g., Jung et al. 2010; Ryzhkov et al. 2011; Snyder 2013; Kumjian et al. 2014; Dawson et al. 2014). Jung et al. (2010), Snyder et al. (2013), and Snyder (2013) used a forward operator combined with a high-resolution numerical model with multimoment bulk microphysics to examine the microphysical composition and structure of simulated Z_{DR} columns. To avoid some of the limitations associated with bulk microphysics, Kumjian et al. (2012) examined drop freezing in a simulated updraft using a one-dimensional spectral bin scheme and detailed the microphysical composition of a resulting Z_{DR} column; liquid and partly liquid freezing

drops associated with a Z_{DR} column were found at greater altitudes as updraft intensity (i.e., vertical velocity w) increased and as the median drop diameter of the distribution of drops decreased. Using the Hebrew University Cloud Model (HUCM), a high-resolution numerical model with spectral bin microphysics, and the polarimetric emulator described in Ryzhkov et al. (2011), Kumjian et al. (2014) showed that realistic simulations of Z_{DR} columns were reproduced when a freezing drop hydrometeor species was added to complement the traditional rain and hail categories. In that paper, the inclusion of freezing drops allowed HUCM to better simulate the physical process of raindrop freezing and the interactions between freezing drops, raindrops, and hail that occur within Z_{DR} columns. This study uses a similar version of the HUCM simulation presented in Kumjian et al. (2014) to describe briefly the structure of simulated Z_{DR} columns and detail why operational meteorologists may find value in examining Z_{DR} columns.

The microphysics scheme within HUCM uses 43 mass-doubling bins to predict the evolution of liquid water (from cloud droplet size to raindrop size), freezing drops, hail, graupel, cloud ice, snow aggregates, and three types of ice crystals (columns, needles, and dendrites). Time-dependent melting of hail, graupel, and snow is modeled; the model includes time-dependent freezing of water accreted on graupel and hail, and the liquid water fractions on hail, graupel, and freezing drops are explicitly predicted (as is the snow rime factor). Freezing drops are modeled as having a liquid water core with an ice shell; melting hail, graupel, and snow are modeled as having an ice core with a liquid water shell. The forward radar operator calculates the scattering amplitudes for hydrometeors using T-matrix calculations for resonance-sized particles and Rayleigh equations for smaller particles. More details on the emulator are provided in Ryzhkov et al. (2011); more details on HUCM and its microphysics scheme can be found in Khain and Sednev (1995), Pinsky et al. (2001), Khain et al. (2001, 2004, 2011, 2013), Phillips et al. (2007, 2014, 2015), Benmoshe et al. (2012), and Kumjian et al. (2014).

For this study, HUCM is used to perform a two-dimensional simulation with vertical grid spacing of 100 m and horizontal grid spacing of 300 m; the model domain is 19 km in vertical and 150 km in horizontal extent. The simulation is run for 7200 s with relevant data written every 60 s. The initial conditions for the simulation are horizontally homogeneous and are based upon the thermodynamic sounding presented in Fig. 3; an initial convective storm is generated by a thermal perturbation. The environmental 0°C level is near
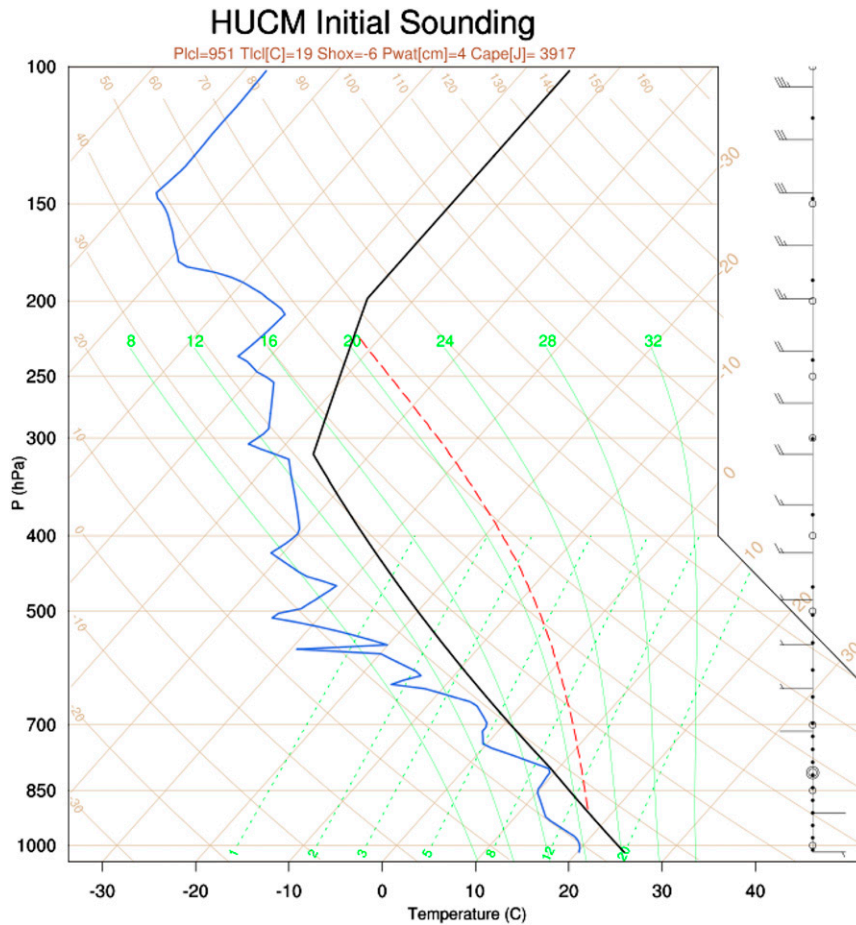
HUCM Initial Sounding

Plcl=951 Tlcl[C]=19 Shox=-6 Pwat[cm]=4 Cape[J]= 3917

FIG. 3. A skew T–log$p$ plot of the initial environmental sounding used in the HUCM simulation with temperature (black), dewpoint temperature (blue), and surface parcel trace (red). Wind barbs (m s^{-1}) are plotted on the right; short and long barbs represent 2.5 and 5.0 m s^{-1} wind speeds, respectively.

3.25 km AGL, and an undiluted surface parcel (red trace in Fig. 3) crosses the 0°C mark at a height of ~4.5 km AGL. Radar variables are calculated as described in Ryzhkov et al. (2011) and, as presented here, are valid at S band (i.e., 10.9-cm wavelength).

During the course of the simulation, several convective storms with peak updraft velocities exceeding 40 m s^{-1} are produced. Associated with the development of each of these updrafts are well-defined Z_{DR} columns. Figure 4 provides an overview of the distribution and characteristics of rain, freezing drops, and hail within one such Z_{DR} column near time $t = 6000$ s. At this time, the 1-dB Z_{DR} contour (purple contour in Fig. 4) extends to approximately 6 km AGL. The reflectivity contribution of rain to the total Z_H is greater than 50% for that part of the Z_{DR} column below ~4.25 km AGL (see Z_{frac}^{rain} in Fig. 4a), although the mass of rainwater relative to total precipitation mass only exceeds 50% at heights below ~3 km AGL (Fig. 4b).

The contribution from freezing drops to the total Z_H increases above ~4.5 km AGL (see Z_{frac}^{fd} in Fig. 4c), although it never exceeds ~40% despite the fact that most of the precipitation mass within the center of the Z_{DR} column from ~4 to ~5.5 km AGL is freezing drops (Fig. 4d). Along the left side of the Z_{DR} column and above ~4.5 km AGL, Z_H is dominated by contributions from wet hail (Fig. 4e), although only along the periphery of the Z_{DR} column is most of the mass actually hail (Fig. 4f). In general, Z_{DR} in hail is proportional to the mean water fraction of the hail (Figs. 4e,f), so it is not surprising that the periphery of the Z_{DR} column is generally composed of relatively dry hail.

These results are summarized in Fig. 5. The Z_{DR} column extends to temperatures of approximately −15°C along primarily the upshear (i.e., left) side of the updraft. Most of the hydrometeor mass in the lower part of the column is rain (Fig. 5b). As the updraft carries the rainwater upward, freezing commences, and the raindrops
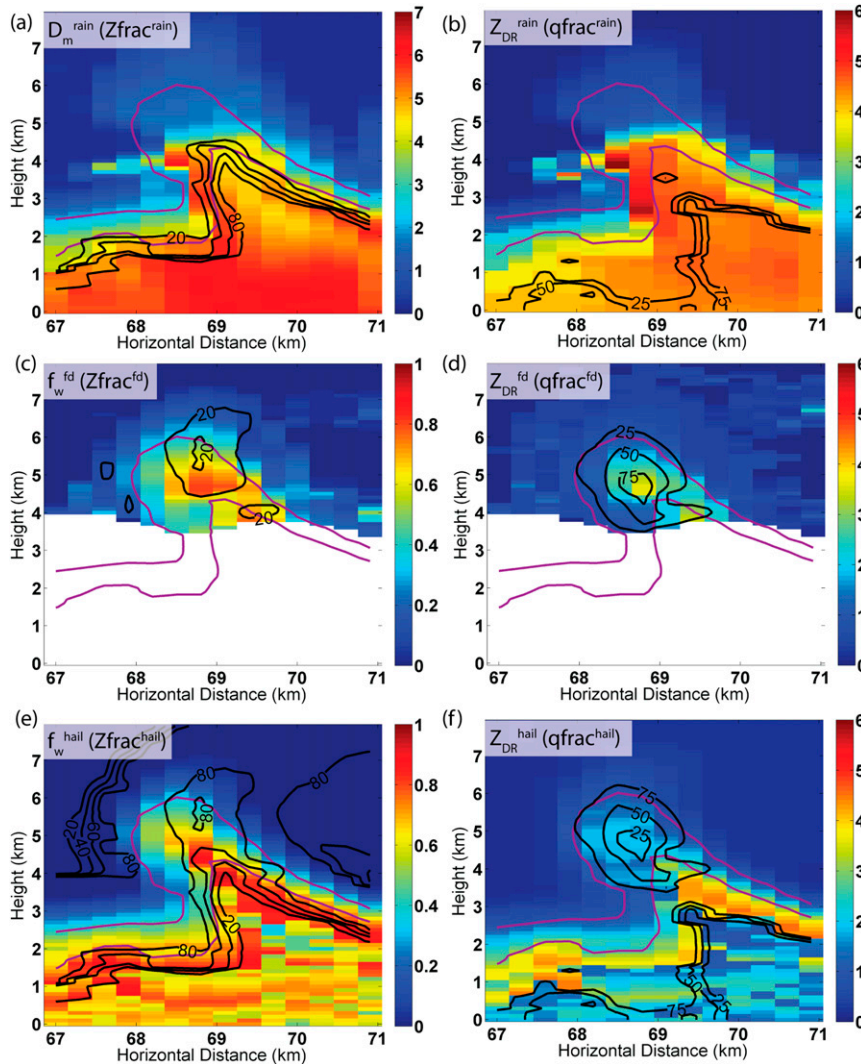
FIG. 4. Selected microphysical characteristics of the Z_{DR} column produced in the HUCM simulation at $t = 6000$ s: (a) mean-mass diameter of rain D_m^{rain} (mm; colored) and rain contribution to total Z_H Z_{frac}^{rain} (%; contours with an interval of 20%), (b) Z_{DR} of rain Z_{DR}^{rain} (dB; colored) and rain contribution to total precipitation mass q_{frac}^{rain} (%; contours with an interval of 25%), (c) mass water fraction of freezing drops f_w^{fd} (%; colored) and freezing drop contribution to the total Z_H Z_{frac}^{fd} (%; contours with an interval of 20%), (d) Z_{DR} of freezing drops Z_{DR}^{fd} (dB; colored) and freezing drop contribution to total precipitation mass q_{frac}^{fd} (%; contours with an interval of 25%), (e) mass water fraction of hail f_w^{hail} (%; colored) and hail contribution to total Z_H Z_{frac}^{hail} (%; contours with an interval of 20%), and (f) Z_{DR} of hail Z_{DR}^{hail} (dB; colored) and hail contribution to total precipitation mass q_{frac}^{hail} (%; contours with an interval of 25%). The purple contours mark 1- and 3-dB Z_{DR}. Mass water fractions are defined as the proportion of the mass of water to the total mass of the particles. For example, f_w^{hail} of 50% means that 50% of the mass of the hail is from liquid water (the other 50% of the mass is ice).

are transferred to the freezing drops category; freezing drops therefore dominate the total mass at the middle altitudes of the column. Eventually, the freezing drops freeze completely and become hail, the mass of which dominates the upper altitudes of the Z_{DR} column. This overall distribution of hydrometeors in and around the Z_{DR} column in this simulation is very consistent with the

storm simulated in Kumjian et al. (2014). Note that a significant part of the downshear (i.e., right) side of the updraft has extremely low liquid water mass; the dearth of liquid water (be it in the form of raindrops, freezing drops, or wet hail) in this part of the updraft results in comparatively low Z_{DR} relative to that in the Z_{DR} column.
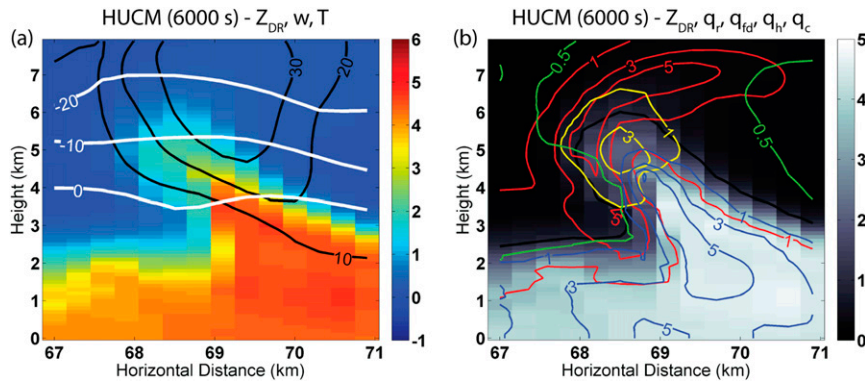
FIG. 5. Results of (a) Z_{DR} (dB; colored), w (m s^{-1}; contours in black with an interval of 10 m s^{-1} starting at 10 m s^{-1}), and air temperature (°C; contours in white at 0°, -10°, and -20°C) show the general relationship between the Z_{DR} column and the updraft. (b) The general microphysical mass composition of the Z_{DR} column (dB; grayscale) for rain (blue contours), freezing drops (yellow contours), and hail (red contours) every 2 g m^{-3} starting at 1 g m^{-3}. The 0.5 g m^{-3} cloud water contour is shown in green.

Figure 6 presents a coarse overview of several convective storm updrafts that are captured during a 1440-s time period near the end of the 7200-s HUCM simulation. By comparing the spatial association between the updrafts (contoured in black every 10 m s^{-1} starting at 10 m s^{-1}) and Z_{DR} (Fig. 6, top), it becomes obvious that developing and mature updrafts (e.g., those associated with $w > 10$ m s^{-1} below 4 km AGL) are associated with upward perturbations in enhanced Z_{DR} [i.e., Z_{DR} columns, the three of which are marked by white letters A, B, and C in Fig. 6 (top)]. Even looking at only the five times presented in Fig. 6, it is apparent that the deepest Z_{DR} columns tend to be associated with the most intense

updrafts, at least when examining w near 4 km AGL. In contrast, the relationship between Z_H (Fig. 6, bottom) and w near 4 km AGL is considerably less clear. Since it takes time to develop hydrometeor distributions with large mass and size (both of which will affect Z_H), there tends to be a lag between the intensification of an updraft and the appearance of high Z_H aloft. Likewise, when updrafts begin to weaken, the hydrometeors associated with high Z_H near an updraft take time to fall to the ground, and so high Z_H aloft tends to persist after the updraft weakens.

In general, there is a robust relationship between the maximum height of each Z_{DR} column and the maximum
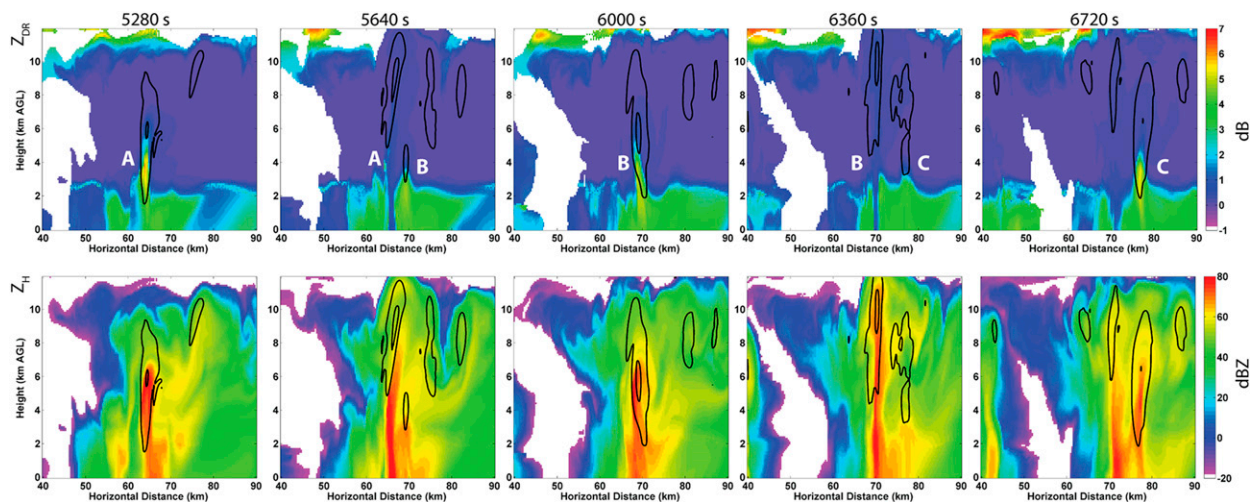

FIG. 6. Results of (top) Z_{DR} and (bottom) Z_H from the HUCM simulation at five different times between 5280 and 6720 s every 360 s. Upward vertical velocities are contoured in black at 10 and 30 m s^{-1}. White letters A, B, and C at top mark three different Z_{DR} columns that occur during the represented time period.
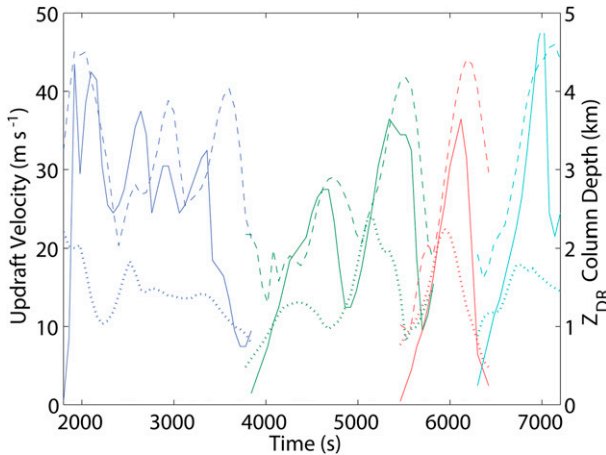
FIG. 7. A time trace of the max Z_{DR} column depth (km; solid lines, above the environmental 0°C level), max w at ~4 km AGL (m s^{-1}; dotted lines), and max w at any height (m s^{-1}; dashed lines) associated with four distinct Z_{DR} columns in the HUCM simulation between 1800 and 7200 s. The Z_{DR} columns marked in green, red, and cyan correspond to those marked by white letters A, B, and C in Fig. 6.

TABLE 1. Correlation coefficients between max Z_{DR} column height and max w associated with the Z_{DR} columns at five time lags between 0 s and four time steps (i.e., 240 s) for the four primary Z_{DR} columns simulated by HUCM (where each letter represents a different colored line segment in Fig. 7). A positive time lag means that the Z_{DR} column heights at an earlier time are being correlated with the max w at a later time. The bold represents the time lag at which the correlation coefficient is maximized.

	0 s	60 s	120 s	180 s	240 s
A	**0.16**	0.04	−0.05	−0.15	−0.21
B	0.73	0.89	**0.92**	0.82	0.63
C	0.64	0.84	**0.95**	0.93	0.77
D	0.81	0.87	**0.92**	0.90	0.87

w both above each column and near the base of each column (Fig. 7). Table 1 contains the correlation coefficients between the maximum Z_{DR} column depth and the maximum w at any height above each Z_{DR} column; Table 2 shows the correlation coefficients between the maximum Z_{DR} column depth and maximum w at 4 km AGL. With the exception of the initial Z_{DR} column, which has a complex evolution that includes at least two periods of weakening and reintensification, the correlation coefficients for Z_{DR} columns B, C, and D range from 0.64 to 0.81. The correlation coefficients are maximized between 0.92 and 0.95 for these three columns at 120-s lag time. In other words, changes in the height of the Z_{DR} columns preceded changes in maximum updraft intensity, a relationship that fits the conceptual model of Z_{DR} columns as follows. With the level of free convection for surface parcels well below the environmental 0°C level, new updrafts ingesting near-surface parcels will develop first at low levels. As the parcels rise, large positive buoyancy supports increasing vertical velocity. In the time it takes for the drops to freeze entirely above the environmental 0°C level (i.e., for the rain to become small hailstones), they are lofted to heights well above 0°C, supporting a deepening Z_{DR} column. Eventually, all of the rain within the parcel freezes, and the Z_{DR} column stops deepening, even if the parcels continue to accelerate upward owing to positive buoyancy. As shown in Kumjian et al. (2014), the large mass of hail aloft that begins from the frozen raindrops lofted in the Z_{DR} column may proceed to fall to the ground, which can reduce the depth of the Z_{DR} column as a result of

increased depletion of supercooled water by hailstone collection or of a weakening of the updraft. If a change in the thermodynamic properties of the inflow parcels (i.e., the inflow temperature decreases) causes an updraft to weaken, one would expect that the Z_{DR} column would become shallower as the lower part of the updraft weakens before the effects of the change in parcel buoyancy are observed at the height of the maximum updraft velocity. As a result, one may observe a change in the depth of the Z_{DR} column before the maximum updraft intensity changes.

Although not the focus of this paper, there is also a high correlation between the depth of the K_{DP} columns and maximum w above the K_{DP} columns. Calculating K_{DP} can be difficult, however; traditional methods for estimating K_{DP} (e.g., as the range derivative of Φ_{DP}) tend to yield noisy K_{DP} in low rain rates. In addition, the presence of a nontrivial backscatter differential phase and gradients therein associated with non-Rayleigh scattering behaviors can artificially increase or decrease K_{DP} if not properly detected and removed before K_{DP} is calculated. The oscillatory nature of K_{DP} when differential phase changes only slow with range is quite evident, for example, in Fig. 1c, which can significantly complicate the quantification of K_{DP} columns. At higher radar frequencies

TABLE 2. As in Table 1, but for the correlation coefficients between max Z_{DR} column heights and max w at 4 km AGL associated with the Z_{DR} columns at five lag times between 0 s and four time steps (i.e., 240 s) for the four primary Z_{DR} columns simulated by HUCM (where each letter represents a different colored line segment in Fig. 7). A negative time lag means that the Z_{DR} column heights at a later time are being correlated with the max w at an earlier time.

	0 s	−60 s	−120 s	−180 s	−240 s
A	0.23	0.52	**0.78**	0.64	0.51
B	0.43	0.67	**0.84**	0.93	0.87
C	0.76	0.92	**0.97**	0.81	0.44
D	0.78	0.83	**0.85**	0.79	0.69

(e.g., X band), where differential attenuation can be much more severe and K_{DP} may be easier to estimate, K_{DP} columns may be a viable alternative to Z_{DR} columns for examining updrafts, although the microphysical compositions of the two signatures are not identical.

3. Algorithm description and Z_{DR} column detection challenges

The Z_{DR} column algorithm outlined in this paper estimates the depth of Z_{DR} columns in polarimetric radar observations. The algorithm has been added to a development version of the Warning Decision Support System–Integrated Information (WDSS-II; Lakshmanan et al. 2006, 2007), and this software is used to create many of the figures contained herein. All data in this paper were collected at Weather Surveillance Radar-1988 Doppler (WSR-88D) stations. Level 2 radar data are preprocessed in a manner very similar to that used by the WSR-88D product generator; of most relevance, the measured Z_{DR} data are filtered in range by means of a five-range-gate moving average to reduce the noisiness often present in Z_{DR}. The filtered Z_{DR} data are objectively analyzed onto a three-dimensional latitude–longitude–height grid with a grid spacing of 0.0025° × 0.0025° in latitude and longitude and 250 m in height. The environmental 0°C height is provided by hourly 13-km Rapid Refresh (RAP; Brown et al. 2011) analyses, although other sources for the environmental 0°C level may be used [e.g., the Rapid Update Cycle (RUC) model for archived cases before RAP operational implementation on 1 May 2012]. At each horizontal grid point, the number of vertically consecutive grid points with $Z_{DR} \geq 1$ dB above the 0°C level are counted such that the result is the vertically continuous depth of the Z_{DR} column (as defined by $Z_{DR} \geq 1$ dB). A Gaussian filter is used to smooth the output from the Z_{DR} column algorithm.

The algorithm provides a filtered, two-dimensional map of the depth of the Z_{DR} column above the model-provided environmental 0°C level. For all examples shown below, the data will be displayed using colors, where warmer colors indicate deeper Z_{DR} columns.

There are several sources of enhanced Z_{DR} above the 0°C level in areas of convective storms that are not associated with Z_{DR} columns and can create false Z_{DR} column detections. For example, the three-body scatter signature (TBSS; e.g., Zrnić 1987; Wilson and Reum 1988; Lemon 1998)—also known as the hail spike (e.g., Wilson and Reum 1986)—is often characterized by low Z_H that decreases with range from the convective storm, very high Z_{DR}, and low ρ_{hv} (e.g., <0.60) along radials downstream of hail-containing radar volumes (e.g., Hubbert and Bringi 2000; Picca and Ryzhkov 2012;

Kumjian 2013c; Mahale et al. 2014). In addition, depolarization streaks associated with the canting of ice in the presence of strong electrification can also yield radially oriented streaks of enhanced Z_{DR} in data from radars that transmit–receive linear, orthogonal polarizations simultaneously (e.g., Ryzhkov and Zrnić 2007; Kumjian 2013c; Hubbert et al. 2014). In both of these cases, the algorithm needs to ignore affected gates to reduce false detections. The initial version of this algorithm attempts to mitigate TBSS contamination by removing radar gates with ρ_{hv} less than approximately 0.80. In the future, explicit detection and removal of the TBSS using a method similar to Mahale et al. (2014) may be required to reduce errors caused by this artifact.

Since this algorithm uses a fixed 1-dB threshold for defining the periphery of a Z_{DR} column, errors in radar calibration can detrimentally affect the performance of the algorithm. True Z_{DR} column depth will be underestimated if a radar has a negative Z_{DR} bias and will be overestimated if there is a positive Z_{DR} bias. In addition, errors in the model analysis of the 0°C height will affect the output from the algorithm.

There is at least one nonmicrophysical source for reduced Z_{DR} aloft within the updraft of convective storms that can detrimentally affect Z_{DR} column detection: tornado debris. The polarimetric tornado debris signature (e.g., Ryzhkov et al. 2005; Kumjian and Ryzhkov 2008; Petersen et al. 2008; Palmer et al. 2011; Schultz et al. 2012; Bluestein et al. 2007a,b, 2012; Snyder et al. 2010; Tanamachi et al. 2012; Bodine et al. 2013; Van Den Broeke and Jauernic 2014; Snyder and Ryzhkov 2015) is typically characterized by moderate-to-high Z_H, low Z_{DR}, and low ρ_{hv} collocated with a strong vortex couplet in radial velocity V_R and is caused by the radar sampling debris lofted by a tornado. In observations of intense tornadoes examined during the course of this research, debris can be carried to heights above the environmental 0°C level within the updraft of the convective storm (e.g., Bodine et al. 2013; Van Den Broeke and Jauernic 2014) and can mask the Z_{DR} column. Mitigation of the masking effect of lofted debris on the Z_{DR} column may require an objective detection of the tornado debris signature (Snyder and Ryzhkov 2015) and likely is only possible if the Z_{DR} column extends above the maximum height of the debris. The current version of the algorithm discussed herein, owing to the vertical continuity requirement, is not designed to find the top of the Z_{DR} column when enough lofted debris is located within the Z_{DR} column to reduce Z_{DR} to less than 1 dB.

The sampling strategy of the radar can affect how well a Z_{DR} column is detected. Traditionally, many operational weather radars, including WSR-88Ds, have used a stepped-spiral approach to data collection,
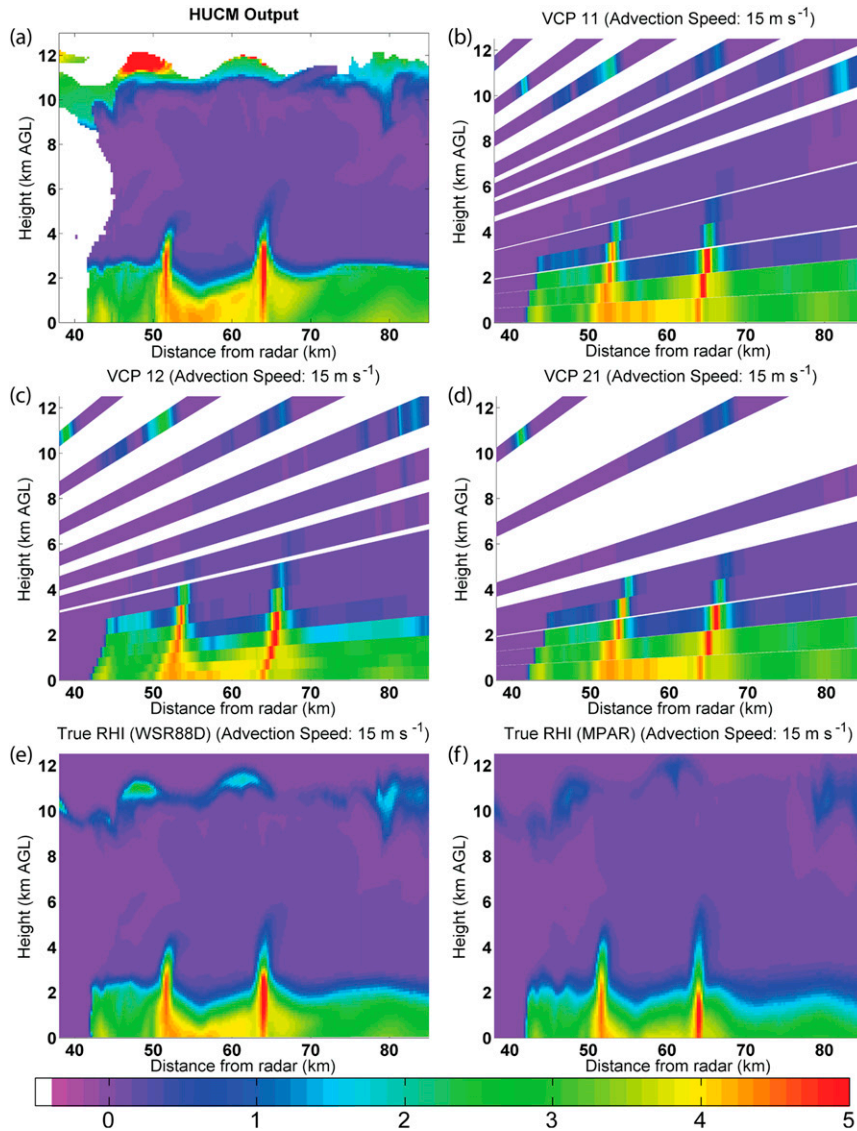
FIG. 8. Simulated reconstructed RHIs of two Z_{DR} columns associated with convective storms in an HUCM simulation using different scanning strategies or VCPs: (b) VCP 11, (c) VCP 12, and (d) VCP 21 from a WSR-88D-like radar. (a) The Z_{DR} columns as produced by the model, and simulated true RHIs from (e) WSR-88D- and (f) MPAR-like radars. The simulated WSR-88D has 0.93° half-power beamwidth with an 8.53-m-diameter antenna and operates at 2.705 GHz. The MPAR-like radar has a 1.6° half-power beamwidth with a 3.3 m × 3.3 m (width × height) square panel operating at 3.12 GHz. Antenna radiation pattern is calculated as in Sherman (1970) and Doviak and Zrnić (1993). All simulated radar images assume that the convective storms are moving from left to right at 15 m s^{-1} and neglect variance in Z_{DR} estimates that arise from finite pulse averaging. Only the 6-dB two-way beamwidth is considered.

wherein a series of plan position indicator (PPI) scans are completed at a set of discrete elevation angles. When convective storms are present within the range of a WSR-88D, the radar will typically be using one of the precipitation mode volume coverage patterns (VCPs; e.g., 11, 12, and 21 or close variants 211, 212, 121, and 221). These VCPs use different sets of elevation angles,

which means that the sampling of Z_{DR} columns may be affected by the chosen VCP. Figure 8 shows how two Z_{DR} columns from the HUCM simulation (Fig. 8a) appear in reconstructed RHIs collected by a simulated WSR-88D using VCPs 11 (Fig. 8b), 12 (Fig. 8c), and 21 (Fig. 8d). The Z_{DR} field is shifted to the right at a constant speed of 15 m s^{-1} to simulate the movement of the
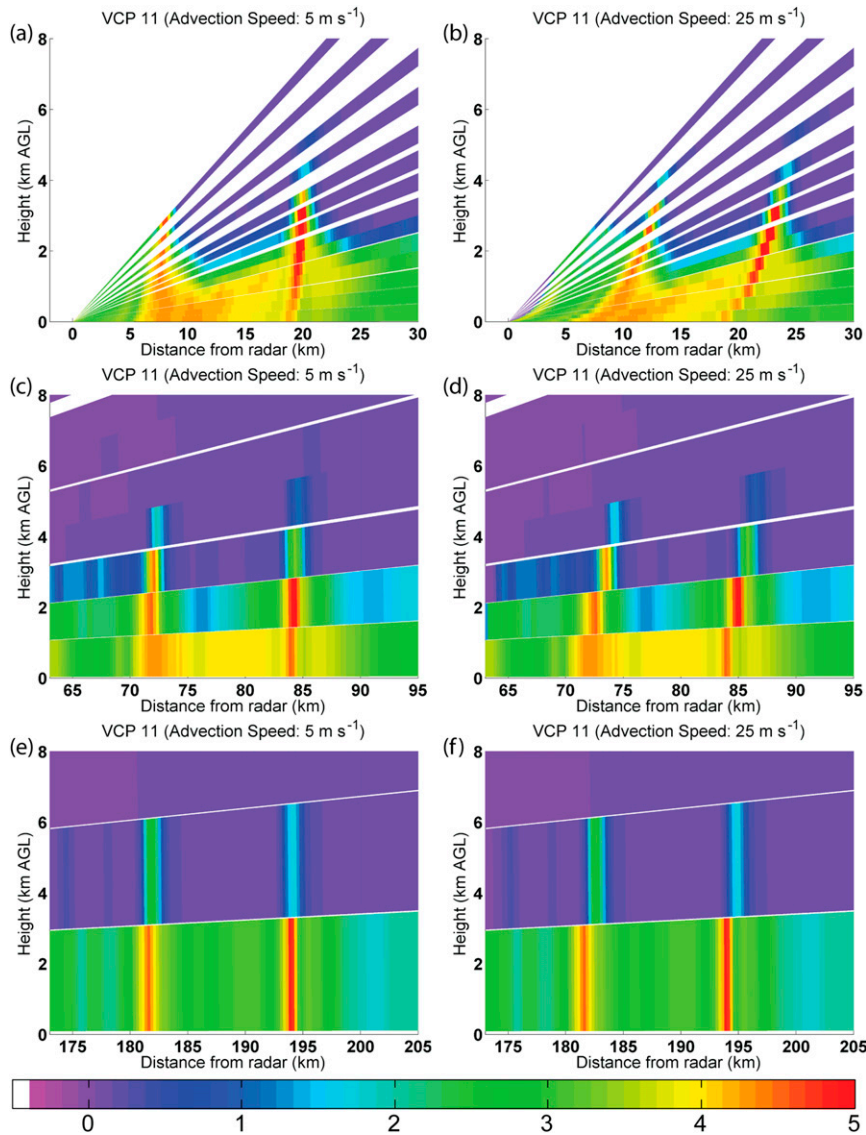
FIG. 9. Simulated reconstructed RHIs from an S-band radar showing two Z_{DR} columns associated with convective storms moving from left to right at (left) 5 and (right) 25 m s^{-1} located approximately (a),(b) 5−25 km from the radar; (c),(d) 70–90 km from the radar; and (e),(f) 180–200 km from the radar. The simulated radar has a 0.93° half-power beamwidth (approximately the same as a WSR-88D) and is scanning using VCP 11, which consists of 16 sweeps at 14 elevation angles from 0.5° to 19.5° and takes approximately 300 s to complete.

convective storms during the course of the data collection volume (this is purely a static translation for illustrative purposes; the field itself does not evolve with time other than via translation). VCP 21 provides comparatively fewer elevation angles above 5°, which results in very poor data coverage above the environmental 0°C level (i.e., ~3.25 km AGL at the ranges represented in Fig. 8). In fact, the Z_{DR} columns are only sampled by two elevation angles with VCP 21 at these ranges. In contrast, true RHIs from a simulated WSR-88D (Fig. 8e) and a simulated multifunction phased-array

radar (MPAR; Weadon et al. 2009; Fig. 8f) better capture the structure of the Z_{DR} columns.

If convective storms are moving quickly, a nontrivial vertical tilt may be introduced into the Z_{DR} columns owing to storm movement during data collection. Preliminary testing indicates that the enforcement of a vertical continuity criterion for Z_{DR} column detection is needed to mitigate false detections and reduce noise in the product, but the use of this criterion can create problems in detecting those Z_{DR} columns that may appear to be tilted owing to storm motion. To illustrate this, Fig. 9

shows two Z_{DR} columns from the HUCM simulation as if they were sampled by a WSR-88D using VCP 11. The left column of Fig. 9 represents Z_{DR} columns that are moving from left to right at $5\,m\,s^{-1}$; the right column of Fig. 9 assumes a speed of $25\,m\,s^{-1}$. VCP 11, for which 16 sweeps of $360°$ are collected at 14 elevation angles, takes approximately 5 min to complete. When the Z_{DR} columns are close to the radar as in Figs. 9a and 9b, the columns are sampled through at least four elevation angles, which means that the Z_{DR} columns move $\sim$180 m (for storm motion u_s of $5\,m\,s^{-1}$) and $\sim$900 m (for u_s of $25\,m\,s^{-1}$) in the $\sim$36-s period that elapses during the collection of those four elevation angles. Depending upon the size of the Z_{DR} columns, the resultant tilt can complicate automated Z_{DR} column depth estimates. When the Z_{DR} columns are farther from the radar (e.g., Figs. 9c–f), the Z_{DR} column is sampled with appreciably lower vertical resolution, but the artificial tilt caused by storm movement during data collection is also reduced. One may also notice that, owing to the $19.5°$ maximum elevation angle used by WSR-88Ds, Z_{DR} columns will appear to become shallower with time as they approach the radar at very short ranges owing to the Z_{DR} column exceeding the uppermost scan; this problem exists for other products that are affected by incomplete storm sampling [e.g., enhanced echo tops (EET) and vertically integrated liquid (VIL)], as will be shown later.

One final note regarding the detectability of Z_{DR} columns: if there are too few sufficiently sized hydrometeors within the updraft of a convective storm, the signal returned to the radar may be too weak for detection. Although Z_{DR} is not sensitive to hydrometeor concentration except in a power-weighted sense when multiple hydrometeor types and sizes are present, the signal must still be strong enough for adequate echo detection and measurement of Z_{DR}.

The relatively poor midtropospheric resolution and coverage associated with the scanning strategies of many operational weather radars complicate Z_{DR} column detection. Developers of technologies such as phased-array radar may want to consider an operation mode whereby a set of RHIs (i.e., data at many elevation angles) are collected at discrete azimuths instead of the traditional stepped-spiral method whereby a set of PPIs (i.e., data at many azimuths) are collected as discrete elevation angles. Scanning in elevation before azimuth will essentially remove artificial tilting caused by data collection delays and will allow for better quantification of Z_{DR} columns.

4. Utilization examples

Several examples of Z_{DR} column algorithm output are shown in this section, although none of these examples

are intended to be detailed analyses of Z_{DR} columns and their associated convective storm. Because the scanning strategies often used to sample convective storms and Z_{DR} columns are not of high vertical resolution, it will become apparent that the algorithm performs best on convective storms with deep Z_{DR} columns, which tend to be associated with supercells in environments of high convective available potential energy (CAPE).

a. Supercells

A series of supercells produced 12 tornadoes within the Norman, Oklahoma, National Weather Service Forecast Office's (NWSFO) County Warning Area (CWA) on the afternoon and evening of 24 May 2011. One such supercell produced at least four tornadoes across central Oklahoma, including a tornado rated as a category 5 event on the enhanced Fujita scale (EF5; Wind Science and Engineering Center 2006). Several radars sampled these supercells (e.g., Houser et al. 2015; Tanamachi et al. 2015); this paper addresses data collected by a research-focused WSR-88D in Norman (KOUN). A sounding from Lamont, located in north-central Oklahoma (LMN), valid near 2100 UTC (Fig. 10), indicates that a lifted surface parcel will cool to $0°C$ approximately 1550 m above the environmental $0°C$ height (within the constraints of parcel theory). As such, one could expect that Z_{DR} columns associated with surface-based convective storms for which the sounding is representative will be at least 1500 m tall. Significant deviations in Z_{DR} column depth above $\sim$1500 m are likely to be attributable to microphysical processes such as noninstantaneous drop freezing.

A view of the supercell at 2055 UTC, near the time of the genesis of a violent tornado (e.g., Houser et al. 2015), is shown in Fig. 11. Although someone familiar with the general structure of supercells may be able to infer the position of updrafts based upon Z_H data (e.g., Figs. 11a, b), details such as updraft intensity and structure typically are not captured in Z_H, particularly at low elevation angles. Turning to Z_{DR}, however, one can identify three primary regions of enhanced Z_{DR} above the environmental $0°C$ level (e.g., at the $4.0°$ elevation angle shown in Fig. 11c). At this particular time, the Z_{DR} column algorithm identifies three large Z_{DR} columns aligned in nearly a north–south fashion. The deepest Z_{DR} column is located near the notch of the hook echo associated with the supercell producing the tornado, whereas the other two Z_{DR} columns are associated with convective storms developing south of and merging into the primary supercell. Tanamachi et al. (2015) examined the mergers experienced by this supercell using a numerical model and assimilating radar data from the MPAR located near KOUN. In their analyses (see their Fig. 13), four updraft
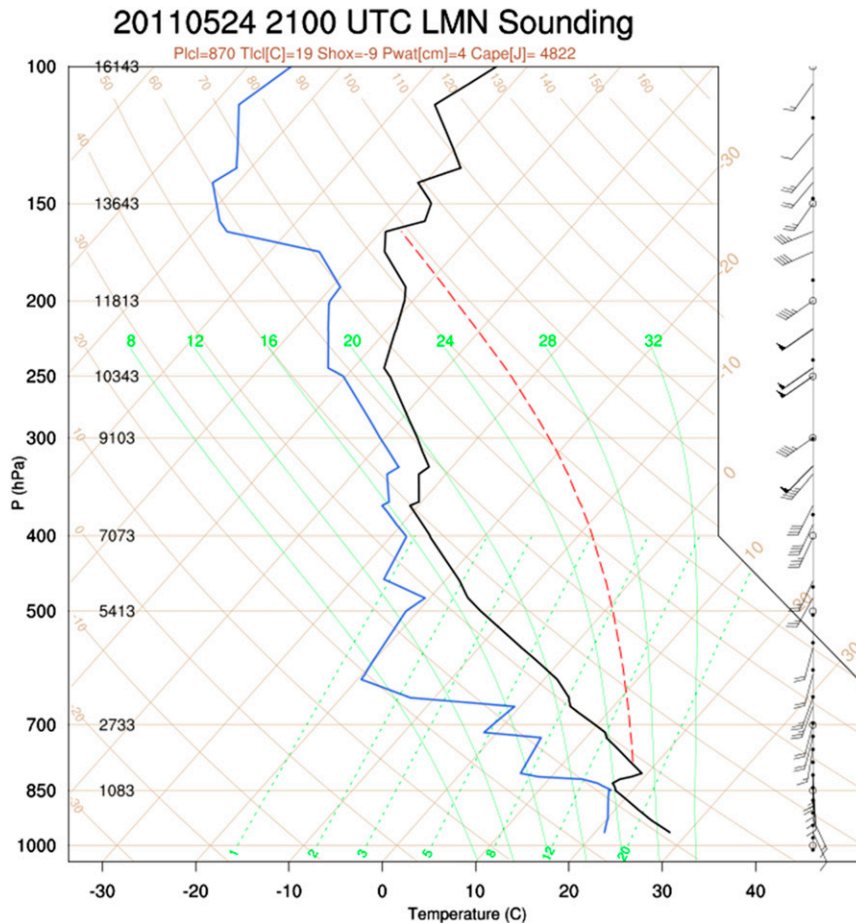
FIG. 10. A skew T–log p plot of the sounding from Lamont at 2100 UTC 24 May 2011 with temperature (black), dewpoint temperature (blue), and surface parcel trace (red). Wind barbs (m s^{-1}) are plotted on the right; only every other wind barb is plotted to reduce clutter. Heights are listed along the mandatory pressure levels (m AGL). The environmental 0°C level is at ~3950 m AGL; the lifted surface parcel cools to 0°C near 5500 m AGL, or ~1550 m above the environmental 0°C level.

elements were produced by the model near this time, although the updrafts in their analysis were aligned more in a northwest–southeast orientation; the strongest updrafts were the northernmost (associated with the supercell) and the southernmost updrafts, which matches quite well with the Z_{DR} column depth estimates that show the northernmost and southernmost Z_{DR} columns to be deeper than the middle Z_{DR} column.

In operational settings, however, analyses such as those in Tanamachi et al. (2015) are not available in real time. The relationship between derived products such as echo tops or EETs (defined as the topmost height of 18.5 dBZ using vertically interpolated Z_H) and VIL and storm intensity as measured by updraft speed or hail production has been previously studied (e.g., Greene and Clark 1972; Edwards and Thompson 1998; Smalley et al. 2003; Lemon 1998; Blair et al. 2011; Lakshmanan

et al. 2013). The accumulated maximum Z_{DR} column depth, EET, and VIL over a 6-h period from 24 to 25 May 2011 are shown in Fig. 12. In general, each of these products produce tracks associated with the path traversed by the convective storms; although they represent very different quantities, the general trends (e.g., maxima) seen in the Z_{DR} column product are also evident in the EET and VIL swaths. However, there are some important differences. For example, the cone of silence near the radar site caused by the 19.5° maximum elevation angle is very noticeable in EET and considerably less evident in Z_{DR} column output and VIL. In addition, VIL is really designed to estimate the total water in a column, and one would not expect the maximum VIL to occur within the updraft of a supercell; Z_{DR}, at least in terms of the Z_{DR} column, is most sensitive to the mean shape of raindrops within the volume,
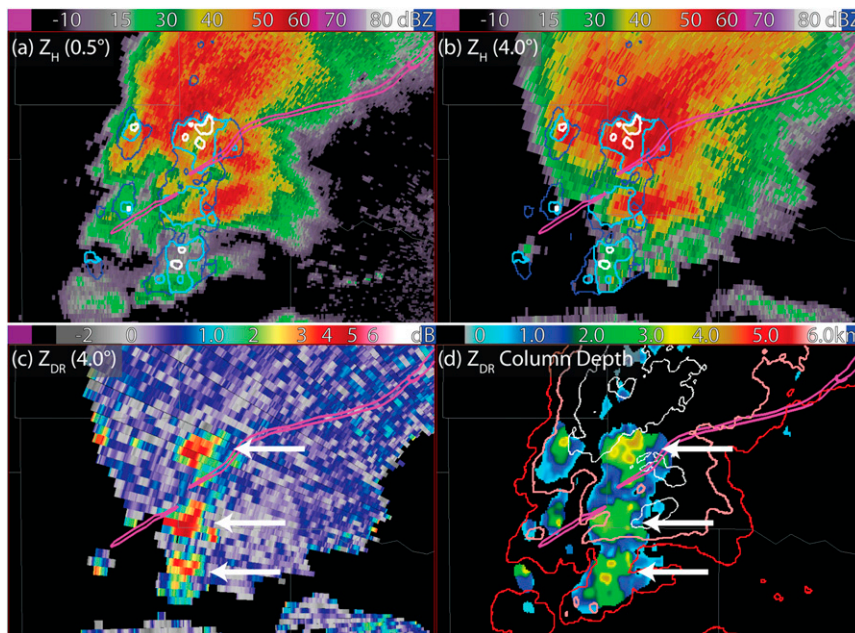
FIG. 11. Data from a supercell near El Reno at ~2055 UTC near the genesis of a violent tornado: (a) Z_H at 0.5° elevation angle (dBZ), (b) Z_H at 4.0° elevation angle (dBZ), (c) filtered Z_{DR} at 4.0° elevation angle (dB), and (d) Z_{DR} column depth provided by the Z_{DR} column algorithm (km; above the environmental 0°C level). Three primary Z_{DR} columns are identified by the algorithm and are noted by white arrows in (c) and (d). The Z_{DR} column depth contours at 1, 2.3, and 3.7 km are marked in dark blue, light blue, and white contours, respectively, in (a) and (b). Contours of Z_H at 10, 30, and 50 dBZ are marked in red, pink, and white, respectively, in (d). The purple swaths are tornado tracks from NWSFO Norman.

not to the total concentration of drops like VIL is. Many of the storms that affected central Oklahoma initiated in the southwestern part of the area covered in Fig. 12, and the very deep Z_{DR} columns noted in the lower-left part of Fig. 12a are associated with the initial development of the deep convection and are maximized near along-storm-track gradients in EET and VIL.

Estimates of storm-top divergence (STD) are available from the Storm Cell Identification and Tracking algorithm (SCIT; Johnson et al. 1998) often used by operational meteorologists with WSR-88D data. Owing to mass conservation, one would generally expect quasi-horizontal divergence near the top of an updraft to be proportional to updraft intensity, all else being equal. If the depth of a Z_{DR} column is proportional to the intensity of an updraft of a convective storm as the previously shown modeling results indicate, we should then expect there to be a direct association between STD and Z_{DR} column depth. Indeed, as shown in Fig. 13, there is a general association between the maximum Z_{DR} column depth, STD, and EET associated with the El Reno, Oklahoma, supercell on 24 May 2011. However, for reasons discussed in section 2, changes in the Z_{DR} column should be sensitive to changes in the updraft within the Z_{DR} column and generally are expected to precede

changes in the maximum updraft intensity (which typically occurs above the Z_{DR} column in common supercell environments). As such, we should expect to see changes in Z_{DR} column depth precede changes in STD and EET. In addition, STD can be prone to errors with velocity dealiasing and cell tracking in SCIT. Finally, since STD and EET often require data taken at heights well above the top of the Z_{DR} column (and thus require data from higher-elevation angles), qualitative examination of Z_{DR} columns is often possible before STD and EET are available for the current radar volume.

Turning to a second case, an intense, extraordinarily large tornado was one of several tornadoes produced by a supercell that occurred in central Oklahoma on the afternoon and evening of 31 May 2013 (e.g., Atkins et al. 2014; Marshall et al. 2014; Bluestein et al. 2015). This supercell was also sampled relatively well by several polarimetric radars (e.g., Snyder and Bluestein 2014; Wurman et al. 2014; Wakimoto et al. 2015), including the WSR-88D at Twin Lakes, southeast of Oklahoma City (KTLX). The thermodynamic sounding nearest this supercell was launched from Norman shortly before 0000 UTC 1 June 2013 (Fig. 14). Owing solely to the warm thermal perturbation associated with latent heating within the updraft of a surface-based convective storm,
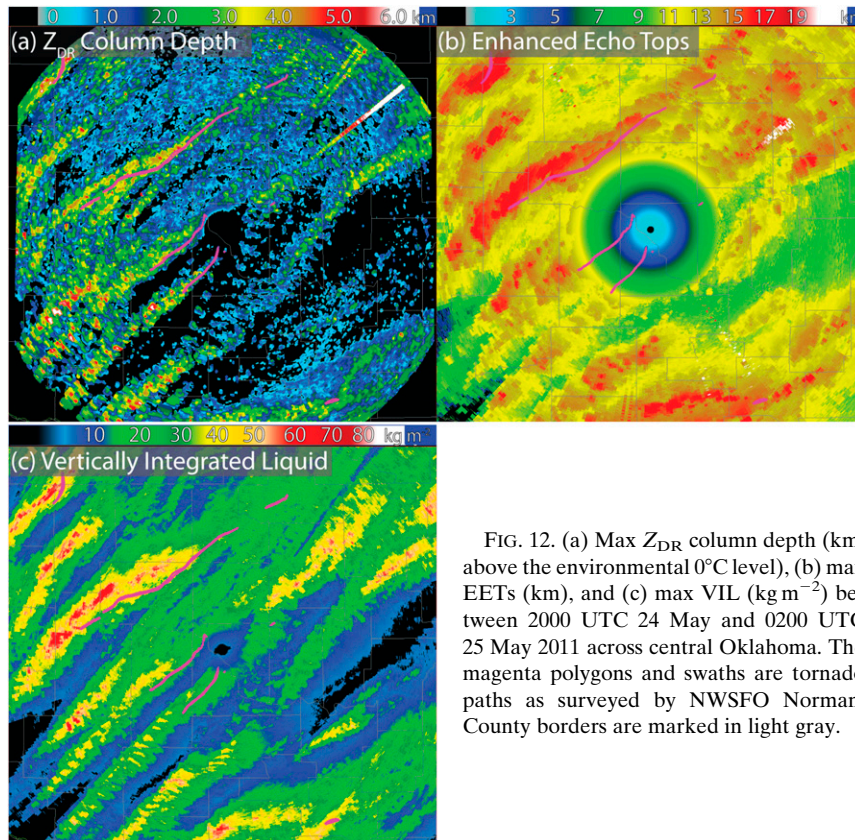
FIG. 12. (a) Max Z_{DR} column depth (km; above the environmental 0°C level), (b) max EETs (km), and (c) max VIL (kg m^{-2}) between 2000 UTC 24 May and 0200 UTC 25 May 2011 across central Oklahoma. The magenta polygons and swaths are tornado paths as surveyed by NWSFO Norman. County borders are marked in light gray.

we would expect Z_{DR} columns to be at least 1600 m tall (the difference in the heights of the lifted surface parcel's 0°C level and the environmental 0°C level).

There is considerable commonality between maximum Z_{DR} column depth and both EET and STD (Fig. 15) for this 31 May 2013 supercell. High volume-to-volume variability in STD is evident, possibly attributable to errors in dealiasing V_R. EET systematically decreases after ~2324 UTC when $Z_H \geq 18.5$ dBZ is sampled at the highest elevation angle (19.5°); as the distance from the supercell to the radar further decreases, the true top of the 18.5-dBZ echo does not get sampled.

As has been stated previously, it is difficult to assess the relationship between Z_{DR} columns and convective storm updrafts using radar data alone owing to the lack of direct observations of updraft intensity and location. The 31 May 2013 case, however, is serving as the focus of an ensemble Kalman filter (EnKF) data assimilation experiment using data from the MPAR (Skinner et al. 2014). As with the comparison of the 24 May 2011 Z_{DR} columns to the analyses by Tanamachi et al. (2015), this should not be used as a true verification since the model is not errorless. However, there does appear to be some agreement between the locations of the primary updraft and the Z_{DR} column associated with this supercell;

Fig. 16 shows the Z_{DR} column depth between 2300 and 2313 UTC from KTLX (Fig. 16, left) compared to the model's w field retrieved through assimilation of MPAR observations (Fig. 16, right). Although the structure of the Z_{DR} column is not identical to the structure of the updraft in the model, the general shape and location of maxima match quite well. For example, both the Z_{DR} column algorithm and the model w indicate the primary updraft is north of the tornado track (indicated by the thick black polygons) during this period. By the end of ~2313–2315 UTC, both the Z_{DR} column algorithm and the model indicate a crescent-shaped updraft in the same general position. This is particular encouraging given that the data come from independent radars.

To reiterate, one should not expect a perfect match since data assimilation does not yield perfect results, and the observed Z_{DR} columns are unlikely to be collocated exactly with the updrafts. However, Z_{DR} column information can be available in near–real time and thus may provide additional information about storm evolution to operational meteorologists.

b. Nonsupercell convective storms

Owing to the weaker (or absent) nonlinear dynamic contribution to the upward-directed vertical perturbation
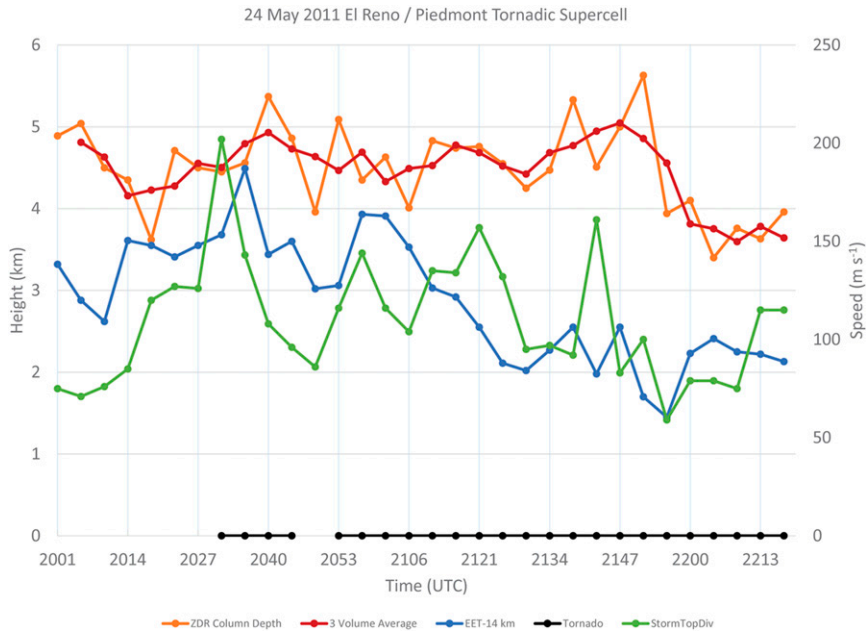
FIG. 13. Time series (with time increasing from left to right as indicated on the abscissa) of max Z_{DR} column depth (km; orange; above the environmental 0°C level) and a three-volume average of max Z_{DR} column depth as calculated from the Z_{DR} column algorithm for a supercell that produced several tornadoes in central Oklahoma during the afternoon of 24 May 2011 (red). Shown for comparison are EETs (km; blue; reduced by 14 km for left ordinate labeling) and max STD (m s^{-1}; green) taken from SCIT (yellow). The black lines along the abscissa represent the times during which tornadoes were occurring with this supercell. Times for the all Z_{DR} column, EET, and STD data are valid at the start of the succeeding radar volume. All data are from KOUN.

pressure gradient force, nonsupercell convective storms tend to have weaker updrafts compared to those associated with supercells. In addition, supercells, at least in the central United States, tend to occur in environments characterized by greater CAPE (e.g., Thompson et al. 2003). As a result, we suspect that Z_{DR} columns associated with nonsupercell storms will tend to be shallower than those associated with supercells, increasing the difficulty of detection and quantification owing to sampling issues discussed in section 3.

Despite concerns about Z_{DR} column detection owing to inadequate spatial sampling, Z_{DR} column depth can still provide useful information about near-term updraft evolution. For example, the ~30-min evolution of a multicell convective complex over western Florida is shown in Fig. 17; Fig. 17 (top) contains Z_H data at a 0.50° elevation angle, and Fig. 17 (bottom) contains output from the Z_{DR} column algorithm. At ~2219 UTC, a north–south band of 40–50-dBZ Z_H is approaching the coastline from the east. Looking at Z_H, it is very difficult to ascertain where the strongest updrafts are located and where one may expect continued development or maintenance. The Z_{DR} column data at ~2220 UTC contain three main areas where the Z_{DR} column exceeds 0.5 km;

the tallest Z_{DR} column is located near the southern extent of the convective cluster. Approximately 20 min later, at 2237 UTC, Z_H has decreased in the central part of the convective cluster, with the higher Z_H located on the southern and northern parts of the cluster. The Z_{DR} column algorithm output shows that the deepest Z_{DR} columns are located along the northern periphery of the convective complex, indicating that this area may be the preferred location of continued convective development. By ~2252 UTC, the southern 50% of the cluster has weakened, leaving higher Z_H on the northern edge of the convection, where the deepest Z_{DR} columns were located at the previous time. Although this example is only one ~30-min period from one case, it appears that the depth of the Z_{DR} columns provides useful short-term prognostic information relevant to operational meteorologists.

Looking at one final case, an intense bow echo moved across eastern Iowa and adjacent portions of Illinois and Wisconsin on the afternoon of 30 June 2014, producing a swath of 30–40 m s^{-1} wind gusts across eastern Iowa (NCDC 2015). The Z_{DR} columns were observed along the leading edge of the squall line near the Z_H gradient, consistent with the expected locations of updrafts in a
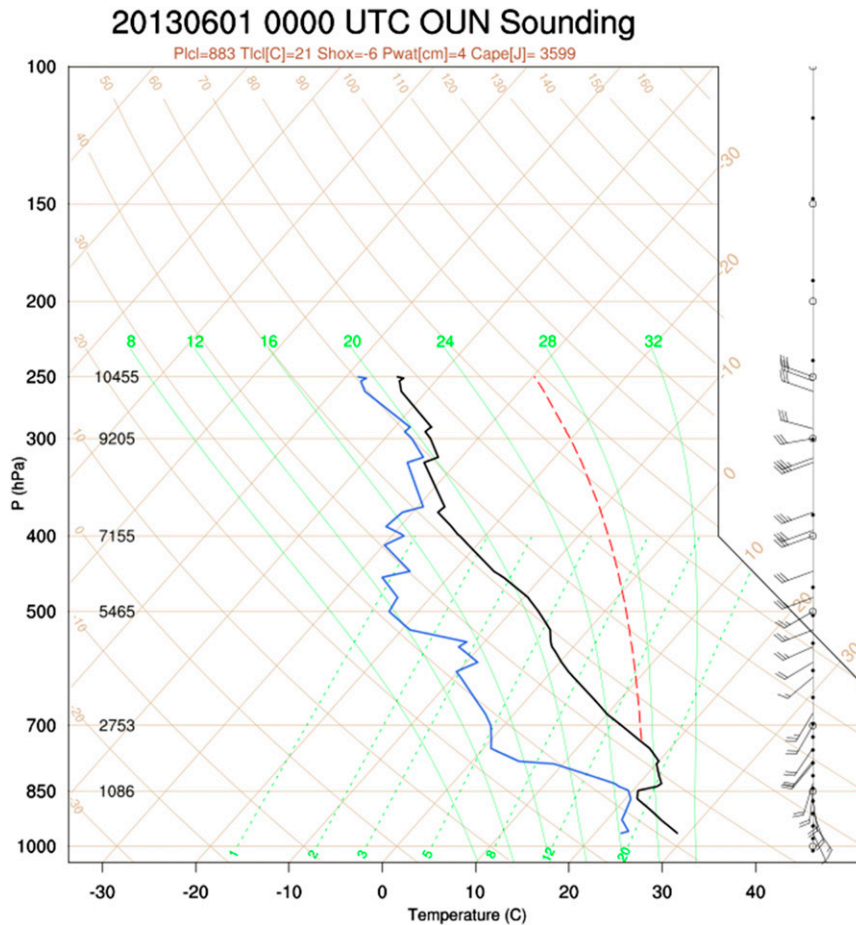
FIG. 14. As in Fig. 10, but for KOUN at 0000 UTC 1 Jun 2013. The environmental 0°C height is ~4300 m AGL; a lifted surface parcel cools to 0°C near 5900 m AGL, or ~1600 m above the environmental 0°C height.

quasi-two-dimensional model of a squall line (e.g., Houze et al. 1989). Relatively early in the event (e.g., ~1930 UTC in Figs. 18a,b), the deepest Z_{DR} columns were located over the southern part of the line, although Z_{DR} column depth exceeded 2.0 km intermittently throughout much of the area ahead of the squall line; Z_H on the lowest elevation angle exceeded 50 dBZ throughout the length of the squall line shown. Approximately 30 min later, the deepest Z_{DR} columns remained over the southern part of the squall line (Fig. 18d), although Z_{DR} columns deeper than 3.0 km were noted along the northern apex of a bowing segment observed in Z_H (Fig. 18c). As the squall line continued to bow out around 2030 UTC, the depth of the Z_{DR} columns along the leading edge of the convection largely diminished to less than 1.0 km (Fig. 18f). In addition, Z_H was decreasing during this time, with Z_H reaching a maximum near 45–50 dBZ in most of the bow echo (Fig. 18e).

Generally, the Z_{DR} columns became shallower and Z_H decreased through the final time presented in Figs. 18g and 18h (2045 UTC). Analyses from the 13-km RAP model (not shown) indicate that the southern extent of the squall line had access to more than 3000 J kg^{-1} of lowest 100 hPa mixed layer CAPE (MLCAPE) at 1900 and 2100 UTC, with MLCAPE less than 2000 J kg^{-1} ahead of the northern part of the squall line. As the squall line moved eastward through eastern Iowa between 1900 and 2100 UTC, the magnitude of the lowest 100-hPa mixed layer convective inhibition (MLCINH) generally increased to >100 J kg^{-1}. These observations are consistent with (i) the deepest Z_{DR} columns accompanying convective updrafts over the southern extent of the squall line (where MLCAPE was greater and MLCINH was lower) and (ii) the squall line weakening with time and eastward extent as MLCINH increased. The convection did continue eastward through northern Illinois and southern Wisconsin for several more hours as destabilization occurred downstream of the convective storms, but the strongest
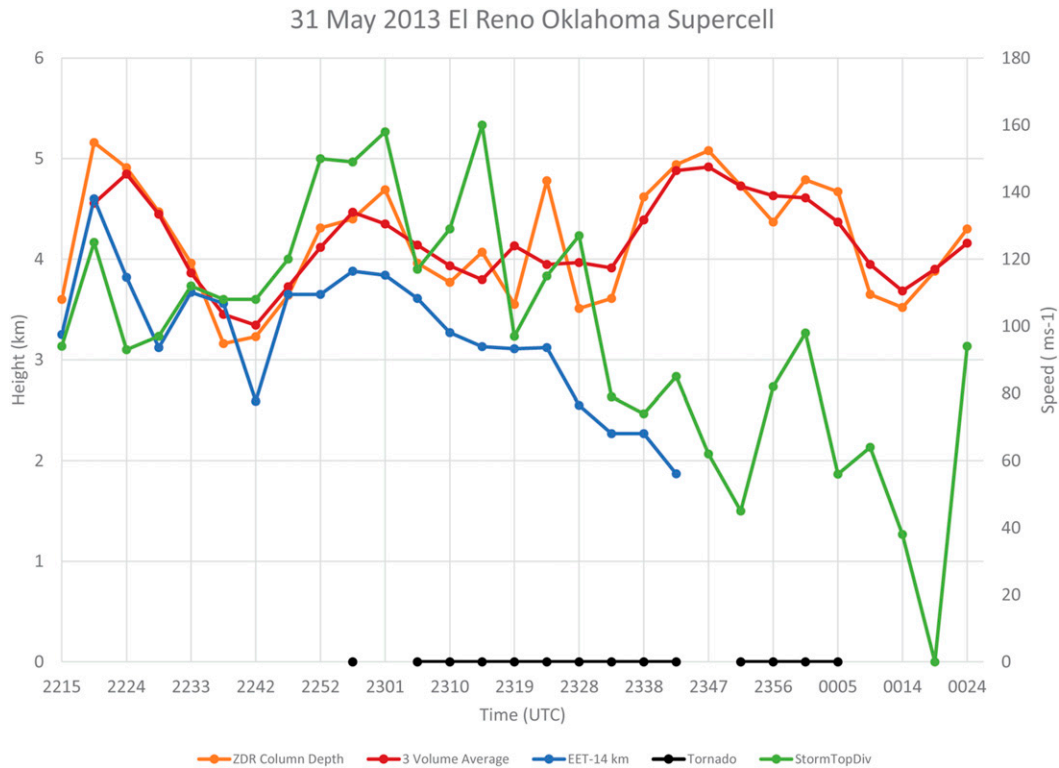
FIG. 15. As in Fig. 13, but for a supercell observed by KTLX from ~2215 UTC 31 May to ~0024 UTC 1 Jun 2013.

near-ground winds occurred in eastern Iowa before 2100 UTC.

5. Conclusions

Analyses from previous observations and results from numerical simulations show a positive spatial relationship between the updraft of convective storms and the Z_{DR} columns associated with those storms. Combining spectral bin microphysics in a high-resolution numerical model with an advanced forward operator, we have shown that the location and depth of the simulated Z_{DR} columns match quite well with the location and intensity of convective storm updrafts, and changes in the maximum vertical velocity within an updraft tend to be seen after changes in the height of a Z_{DR} column. In general, Z_{DR} columns tend to be dominated by rain early in their lives or at lower altitudes when the column is more mature. The raindrops freeze into hail as they rise in the updraft, such that the upper altitudes of the Z_{DR} column tend to be dominated by wet hail. Depending upon the particular environment and evolution of the storm, the hail may fall back through the updraft, weakening the updraft and/or masking the Z_{DR} column (e.g., Kumjian et al. 2014).

Translating what happens in a numerical model to what is observed in the real atmosphere using currently available technology is not always straightforward owing to the differences between the model results or the observational data provided by a radar such as WSR-88D. The analysis of the Z_{DR} column algorithm presented in this paper indicates that Z_{DR} columns may provide near-real-time information on the intensity and location of updrafts, at least for the deeper Z_{DR} columns associated with strong updrafts. Identifying and quantifying Z_{DR} columns may also prove useful in radar data assimilation owing to the ability of the Z_{DR} column to provide valuable information (sometimes in the absence of high Z_H) on latent heating rates and hydrometeor distributions via updraft identification. However, incomplete radar coverage associated with the VCPs used by the WSR-88D network introduces difficulties in detecting and quantifying Z_{DR} column depth, particularly those associated with weaker updrafts or those at particular ranges from the radar (depending upon VCP and the maximum height of the Z_{DR} column). Future Z_{DR} column detection can be improved with the collection of higher-resolution, true RHIs or by the use of a VCP that provides more complete scanning of the atmosphere above the environmental 0°C level.

Note that an algorithm such as that presented herein is not necessary to assess subjectively the Z_{DR} column
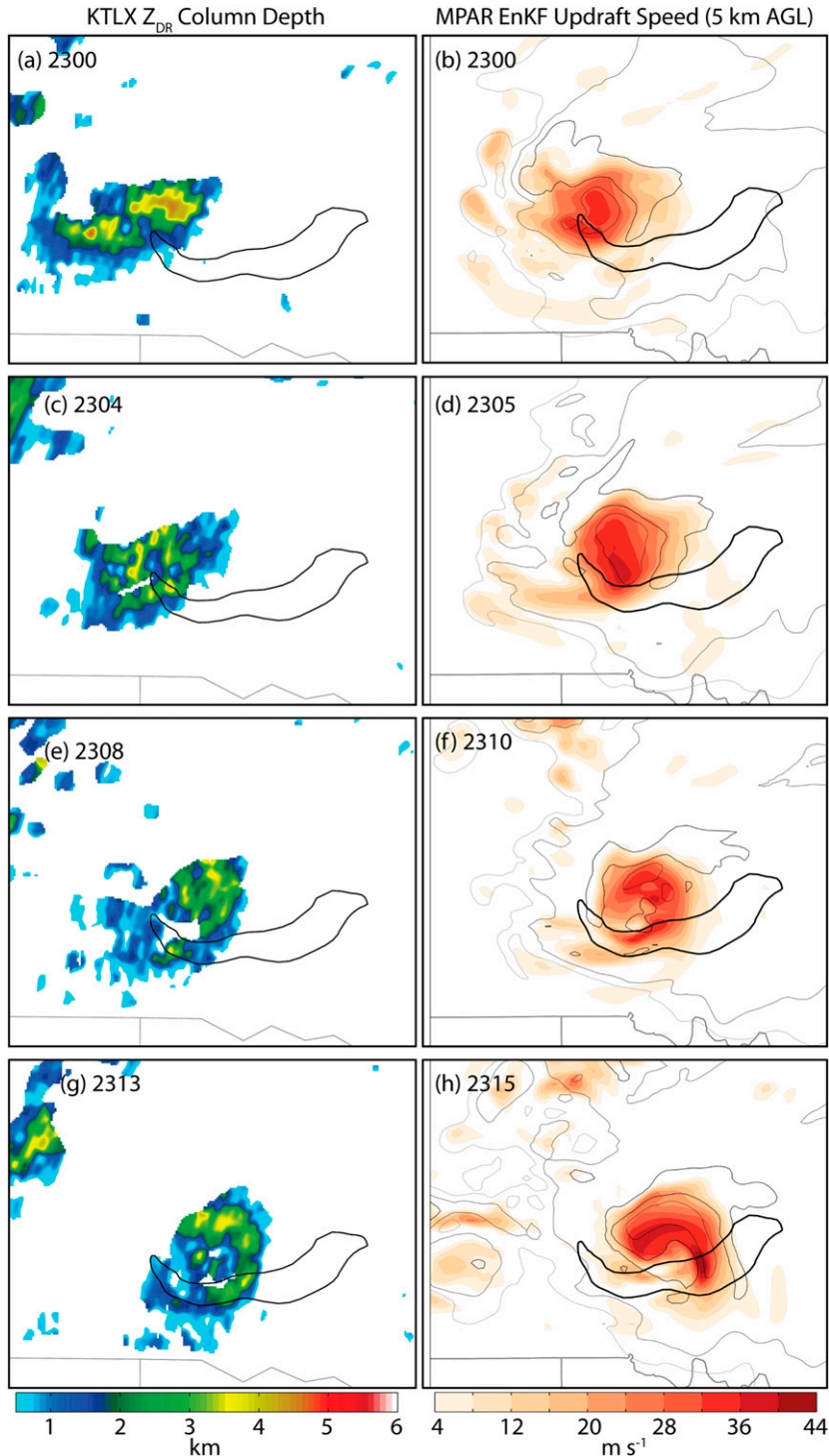
KTLX Z_{DR} Column Depth | MPAR EnKF Updraft Speed (5 km AGL)

FIG. 16. An evolution of the (left) Z_{DR} column depth (km; above the environmental 0°C level) from KTLX and (right) retrieved w (m s^{-1}) at ~5 km AGL from an EnKF data assimilation experiment using independent data from the MPAR (Skinner et al. 2014). In both (a) and (b), dark gray line segments represent the U.S.–Canada border and the black polygon represents the approximate edge of the tornado track as determined by NWSFO Norman. In addition, model reflectivity factor is contoured in the EnKF data. The times marked at left are approximate times of the last elevation angle within a volume that sampled the Z_{DR} column; the times marked at right are times at the center of a 5-min window during which observations from the MPAR were assimilated. (EnKF analysis data are courtesy of P. Skinner.)
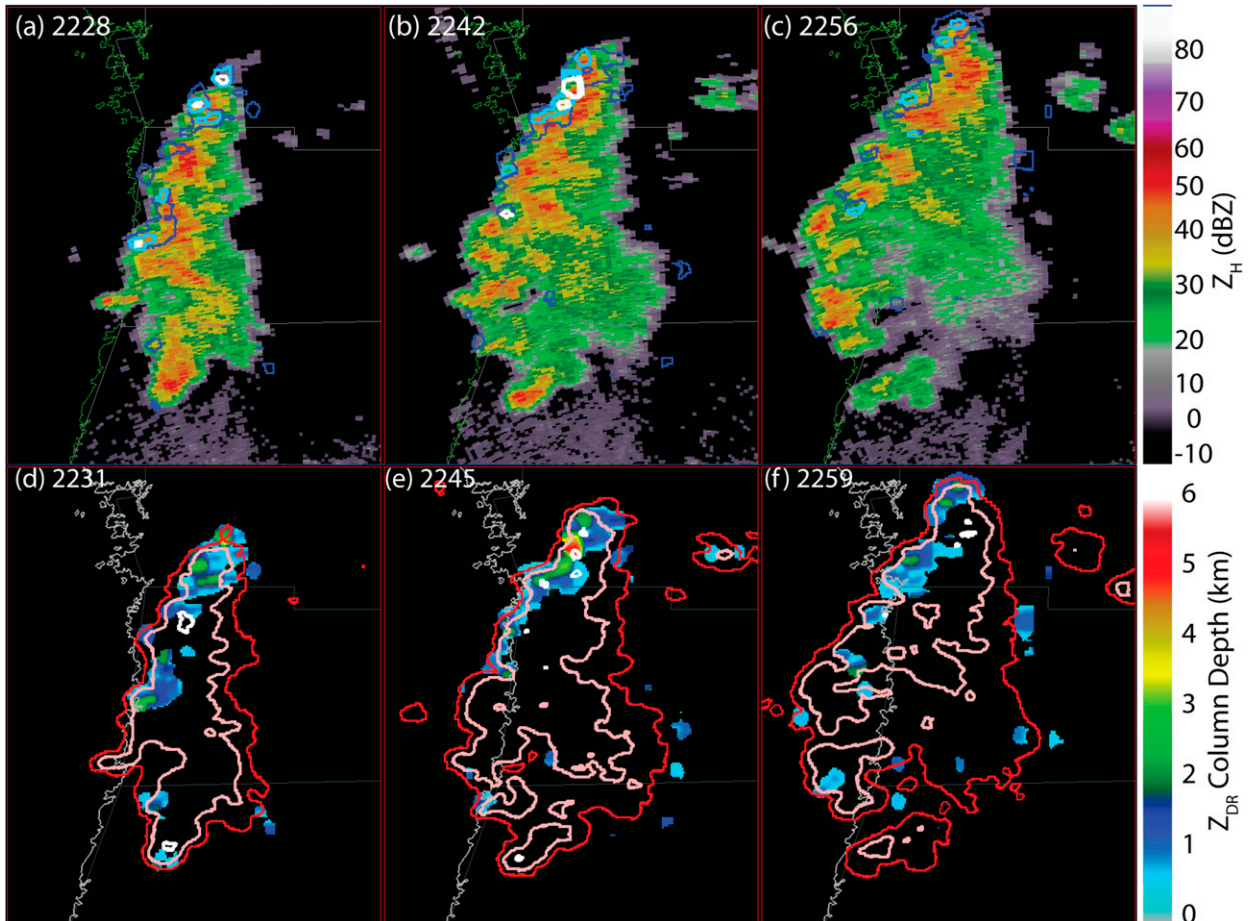
FIG. 17. Time series (with time increasing from left to right) of (a)–(c) Z_H at 0.50° elevation angle and (d)–(f) Z_{DR} column depth from the WSR-88D in Tampa Bay, Florida (KTBW), on the afternoon of 24 Jun 2013. Contours of Z_{DR} column depth of 1, 2, and 3 km are shown in dark blue, light blue, and white, respectively, in (a)–(c); Z_H contours at 10, 30, and 50 dBZ are shown in dark red, pink, and white, respectively, in (d)–(f).

depth on a more limited, case-by-case basis. Depending upon the depth of the Z_{DR} column and the range from the radar, reconstructed RHIs may be used to identify and track Z_{DR} columns; this information can be used to corroborate other radar-derived proxies for updraft intensity or location (e.g., VIL, EET, BWER, etc.) to provide an operational meteorologist with greater confidence that a particular convective storm is weakening or intensifying. For example, if a meteorologist is uncertain whether or not to issue a severe thunderstorm warning on a particular storm owing to marginal assessments using other products (e.g., 50-dBZ echo height), the Z_{DR} column depth and the tendency thereof may prove useful for anticipating the near-term trend in intensity. In addition, knowing the location and structure of the updraft may provide insight into where large hail may be located (even in the absence of high Z_H, since the low number

concentration of very large hail that may fall under or along the periphery of an updraft may be associated with only modest Z_H).

More detailed relations between what changes in Z_{DR} column depth or structure may imply about convective storm evolution or hazardous threat occurrence await future study. For cases in which an automated algorithm such as that discussed herein may not prove particularly useful (e.g., for highly sheared or shallow Z_{DR} columns, for times when the provided 0°C height is incorrect, for regions of enhanced Z_{DR} above the 0°C height that are the result of processes other than those associated with Z_{DR} columns, or for Z_{DR} columns that are masked by the presence of large hail), meteorologists may still be able to examine Z_{DR} subjectively for other signs of updraft presence or evolution. For example, a local increase or maximum in Z_{DR} may be seen within or beneath an updraft as a result of size sorting.
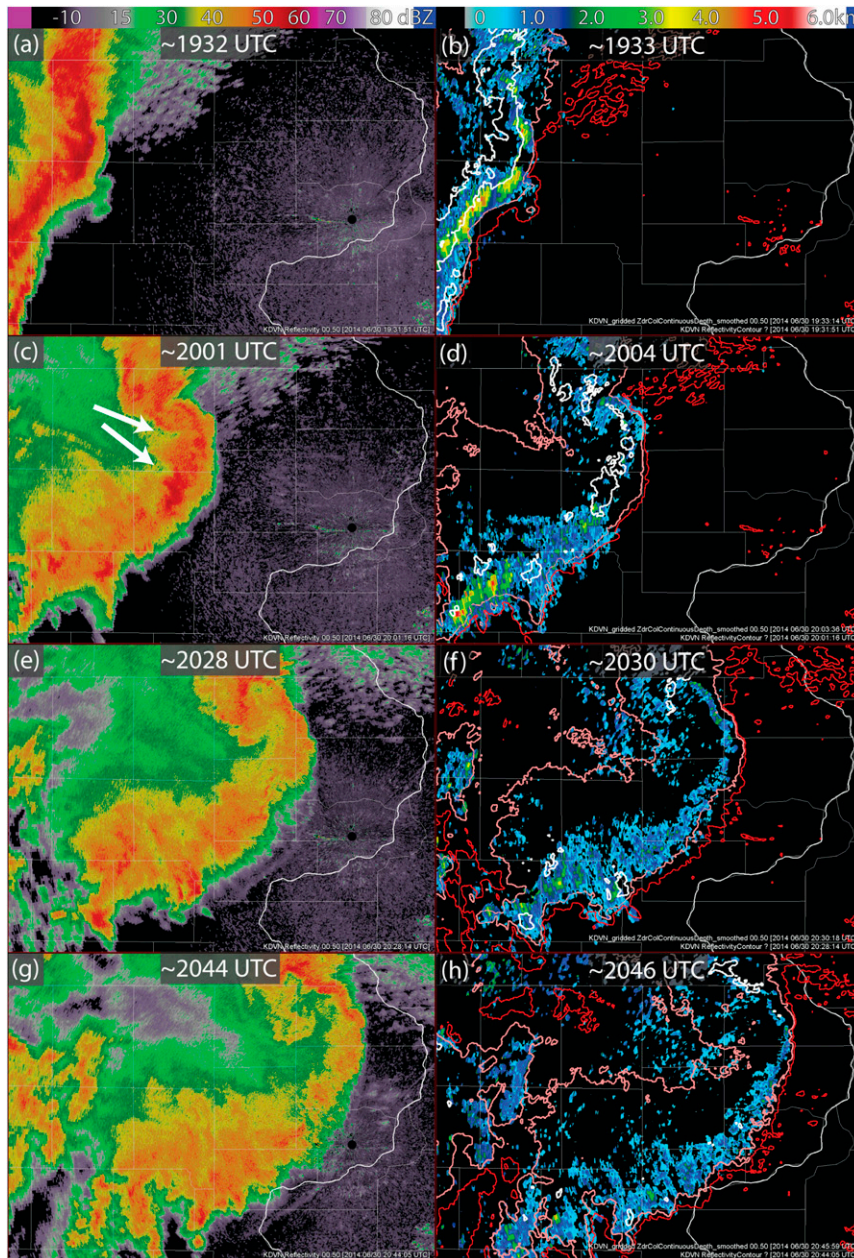
FIG. 18. Results of (left) Z_H at 0.5° elevation angle and (right) output from the Z_{DR} column algorithm from the WSR-88D at Quad Cities, Iowa (KDVN), at approximately (a),(b) 1930; (c),(d) 2000; (e),(f) 2030; and (g),(h) 2045 UTC 30 Jun 2014. The white arrows in (d) highlight potential rear-inflow jets. Contours of Z_H at 10, 30, and 50 dBZ are colored red, pink, and white, respectively (right).

REFERENCES

Atkins, N. T., R. Wakimoto, K. M. Butler, H. B. Bluestein, K. J. Thiem, J. C. Snyder, J. Houser, and J. Wurman, 2014: Aerial damage survey and high resolution dual-polarization radar analysis of the 2013 El Reno tornado. *Proc. 27th Conf. on Severe Local Storms*, Madison, WI, Amer. Meteor. Soc., 13.3. [Available online at https://ams.confex.com/ams/27SLS/webprogram/Paper254162.html.]

Benmoshe, N., M. Pinsky, A. Pokrovsky, and A. Khain, 2012: Turbulent effects on the microphysics and initiation of warm rain in deep convective clouds: 2-D simulations by a spectral mixed-phase microphysics cloud model. *J. Geophys. Res.*, **117**, D06220, doi:10.1029/2011JD016603.

Bigg, E. K., 1953: The formation of atmospheric ice crystals by the freezing of droplets. *Quart. J. Roy. Meteor. Soc.*, **79**, 510–519, doi:10.1002/qj.49707934207.

Blair, S. F., D. R. Deroche, J. M. Boustead, J. W. Leighton, B. L. Barjenbruch, and W. P. Gargan, 2011: A radar-based assessment of the detectability of giant hail. *Electron. J. Severe Storms Meteor.*, **6** (7). [Available online at http://www.ejssm.org/ojs/index.php/ejssm/article/viewArticle/87.]

Bluestein, H. B., M. M. French, R. L. Tanamachi, S. Frasier, K. Hardwick, F. Junyent, and A. L. Pazmany, 2007a: Close-range observations of tornadoes in supercells made with a dual-polarization, X-band, mobile Doppler radar. *Mon. Wea. Rev.*, **135**, 1522–1543, doi:10.1175/MWR3349.1.

——, C. C. Weiss, M. M. French, E. M. Holthaus, R. L. Tanamachi, S. Frasier, and A. L. Pazmany, 2007b: The structure of tornadoes near Attica, Kansas, on 12 May 2004: High-resolution, mobile, Doppler radar observations. *Mon. Wea. Rev.*, **135**, 475–506, doi:10.1175/MWR3295.1.

——, J. C. Snyder, J. B. Houser, and A. L. Pazmany, 2012: Rapid-scan, polarimetric, mobile Doppler radar observations at X-band of an EF-5 tornado in Oklahoma on 24 May 2011. *Extended Abstracts, Seventh European Conf. on Radar in Meteorology and Hydrology*, Toulouse, France, Météo-France, RCS041. [Available online at http://www.meteo.fr/cic/meetings/2012/ERAD/extended_abs/RCS_041_ext_abs.pdf.]

——, ——, and ——, 2015: A multiscale overview of the El Reno, Oklahoma, tornadic supercell of 31 May 2013. *Wea. Forecasting*, **30**, 525–552, doi:10.1175/WAF-D-14-00152.1.

Bodine, D. J., M. R. Kumjian, R. D. Palmer, P. L. Heinselman, and A. V. Ryzhkov, 2013: Tornado damage estimation using polarimetric radar. *Wea. Forecasting*, **28**, 139–158, doi:10.1175/WAF-D-11-00158.1.

Brandes, E. A., and K. Ikeda, 2004: Freezing-level estimation with polarimetric radar. *J. Appl. Meteor.*, **43**, 1541–1553, doi:10.1175/JAM2155.1.

——, J. Vivekanandan, J. D. Tuttle, and C. J. Kessinger, 1995: A study of thunderstorm microphysics with multiparameter radar and aircraft observations. *Mon. Wea. Rev.*, **123**, 3129–3143, doi:10.1175/1520-0493(1995)123<3129:ASOTMW>2.0.CO;2.

Bringi, V. N., and V. Chandrasekar, 2001: *Polarimetric Doppler Weather Radar.* 1st ed. Cambridge University Press, 636 pp.

——, D. A. Burrows, and S. M. Menon, 1991: Multiparameter radar and aircraft study of raindrop spectral evolution in warm-based clouds. *J. Appl. Meteor.*, **30**, 853–880, doi:10.1175/1520-0450(1991)030<0853:MRAASO>2.0.CO;2.

——, L. Liu, P. C. Kennedy, V. Chandrasekar, and S. A. Rutledge, 1996: Dual multiparameter radar observations of intense convective storms: The 24 June 1992 case study. *Meteor. Atmos. Phys.*, **59**, 3–31, doi:10.1007/BF01031999.

——, K. Knupp, A. Detwiler, L. Liu, I. J. Caylor, and R. A. Black, 1997: Evolution of a Florida thunderstorm during the Convection and Precipitation/Electrification Experiment: The case of 9 August 1991. *Mon. Wea. Rev.*, **125**, 2131–2160, doi:10.1175/1520-0493(1997)125<2131:EOAFTD>2.0.CO;2.

Brown, J. M., and Coauthors, 2011: Improvement and testing of WRF physics options for application to Rapid Refresh and High Resolution Rapid Refresh. *Proc. 14th Conf. on Mesoscale Processes/15th Conf. on Aviation, Range, and Aerospace Meteorology*, Los Angeles, CA, Amer. Meteor. Soc., 5.5. [Available online at https://ams.confex.com/ams/14Meso15ARAM/webprogram/Paper191234.html.]

Browning, K. A., 1966: The lobe structure of giant hailstones. *Quart. J. Roy. Meteor. Soc.*, **92**, 1–14, doi:10.1002/qj.49709239102.

——, and R. J. Donaldson, 1963: Airflow and structure of a tornadic storm. *J. Atmos. Sci.*, **20**, 533–545, doi:10.1175/1520-0469(1963)020<0533:AASOAT>2.0.CO;2.

Calhoun, K. M., D. R. MacGorman, C. L. Ziegler, and M. I. Biggerstaff, 2013: Evolution of lightning activity and storm charge relative to dual-Doppler analysis of a high-precipitation supercell storm. *Mon. Wea. Rev.*, **141**, 2199–2223, doi:10.1175/MWR-D-12-00258.1.

Caylor, I. J., and A. J. Illingworth, 1987: Radar observations and modelling of warm rain initiation. *Quart. J. Roy. Meteor. Soc.*, **113**, 1171–1191, doi:10.1002/qj.49711347806.

Chisholm, A. J., 1973: Part I: Radar case studies and airflow models. *Alberta Hailstorms*, *Meteor. Monogr.*, No. 36, Amer. Meteor. Soc., 1–36.

Conway, J. W., and D. S. Zrnić, 1993: A study of embryo production and hail growth using dual-Doppler and multiparameter radars. *Mon. Wea. Rev.*, **121**, 2511–2528, doi:10.1175/1520-0493(1993)121<2511:ASOEPA>2.0.CO;2.

Dawson, D. T., E. R. Mansell, Y. Jung, L. J. Wicker, M. R. Kumjian, and M. Xue, 2014: Low-level Z_{DR} signatures in supercell forward flanks: The role of size sorting and melting of hail. *J. Atmos. Sci.*, **71**, 276–299, doi:10.1175/JAS-D-13-0118.1.

Doviak, R. J., and D. S. Zrnić, 1993: *Doppler Radar and Weather Observations.* 2nd ed. Academic Press, 562 pp.

Edwards, R., and R. L. Thompson, 1998: Nationwide comparisons of hail size with WSR-88D vertically integrated liquid water and derived thermodynamic sounding data. *Wea. Forecasting*, **13**, 277–285, doi:10.1175/1520-0434(1998)013<0277:NCOHSW>2.0.CO;2.

Giangrande, S. E., J. M. Krause, and A. V. Ryzhkov, 2008: Automatic designation of the melting layer with a polarimetric prototype of the WSR-88D radar. *J. Appl. Meteor. Climatol.*, **47**, 1354–1364, doi:10.1175/2007JAMC1634.1.

Greene, D. R., and R. A. Clark, 1972: Vertically integrated liquid water—A new analysis tool. *Mon. Wea. Rev.*, **100**, 548–552, doi:10.1175/1520-0493(1972)100<0548:VILWNA>2.3.CO;2.

Houser, J. L., H. B. Bluestein, and J. C. Snyder, 2015: Rapid-scan, polarimetric, Doppler radar observations of tornadogenesis and tornado dissipation in a tornadic supercell: The "El Reno, Oklahoma" storm of 24 May 2011. *Mon. Wea. Rev.*, **143**, 2685–2710, doi:10.1175/MWR-D-14-00253.1.

Houze, R. A., Jr., S. A. Rutledge, M. I. Biggerstaff, and B. F. Smull, 1989: Interpretation of Doppler weather radar displays of midlatitude mesoscale convective systems. *Bull. Amer. Meteor. Soc.*, **70**, 608–619, doi:10.1175/1520-0477(1989)070<0608:IODWRD>2.0.CO;2.

Hubbert, J. C., and V. N. Bringi, 2000: The effects of three-body scattering on differential reflectivity signatures. *J. Atmos. Oceanic*

Technol., **17**, 51–61, doi:10.1175/1520-0426(2000)017<0051:TEOTBS>2.0.CO;2.

——, ——, L. D. Carey, and S. Bolen, 1998: CSU-CHILL polarimetric radar measurements from a severe hail storm in eastern Colorado. *J. Appl. Meteor.*, **37**, 749–775, doi:10.1175/1520-0450(1998)037<0749:CCPRMF>2.0.CO;2.

——, S. M. Ellis, W.-Y. Chang, S. Rutledge, and M. Dixon, 2014: Modeling and interpretation of S-band ice crystal depolarization signatures from data obtained by simultaneously transmitting horizontally and vertically polarized fields. *J. Appl. Meteor. Climatol.*, **53**, 1659–1677, doi:10.1175/JAMC-D-13-0158.1.

Illingworth, A. J., J. W. F. Goddard, and S. M. Cherry, 1987: Polarization radar studies of precipitation development in convective storms. *Quart. J. Roy. Meteor. Soc.*, **113**, 469–489, doi:10.1002/qj.49711347604.

Jameson, A. R., M. J. Murphy, and E. P. Krider, 1996: Multiple parameter radar observations of isolated Florida thunderstorms during the onset of electrification. *J. Appl. Meteor.*, **35**, 343–354, doi:10.1175/1520-0450(1996)035<0343:MPROOI>2.0.CO;2.

Johnson, D. A., and J. Hallett, 1968: Freezing and shattering of supercooled water drops. *Quart. J. Roy. Meteor. Soc.*, **94**, 468–482, doi:10.1002/qj.49709440204.

Johnson, J. T., P. L. MacKeen, A. Witt, E. D. Mitchell, G. J. Stumpf, M. D. Eilts, and K. W. Thomas, 1998: The Storm Cell Identification and Tracking algorithm: An enhanced WSR-88D algorithm. *Wea. Forecasting*, **13**, 263–276, doi:10.1175/1520-0434(1998)013<0263:TSCIAT>2.0.CO;2.

Jung, Y., M. Xue, and G. Zhang, 2010: Simulations of polarimetric radar signatures of a supercell storm using a two-moment bulk microphysics scheme. *J. Appl. Meteor. Climatol.*, **49**, 146–163, doi:10.1175/2009JAMC2178.1.

Kennedy, P. C., S. A. Rutledge, W. A. Petersen, and V. N. Bringi, 2001: Polarimetric radar observations of hail formation. *J. Appl. Meteor.*, **40**, 1347–1366, doi:10.1175/1520-0450(2001)040<1347:PROOHF>2.0.CO;2.

Khain, A. P., and I. L. Sednev, 1995: Simulation of hydrometeor size spectra evolution by water–water, ice–water and ice–ice interactions. *Atmos. Res.*, **36**, 107–138, doi:10.1016/0169-8095(94)00030-H.

——, M. B. Pinsky, M. Shapiro, and A. Pokrovsky, 2001: Collision rate of small graupel and water drops. *J. Atmos. Sci.*, **58**, 2571–2595, doi:10.1175/1520-0469(2001)058<2571:CROSGA>2.0.CO;2.

——, A. Pokrovsky, M. Pinsky, A. Seifert, and V. Phillips, 2004: Effects of atmospheric aerosols on deep convective clouds as seen from simulations using a spectral microphysics mixed-phase cumulus cloud model. Part I: Model description and possible applications. *J. Atmos. Sci.*, **61**, 2963–2982, doi:10.1175/JAS-3350.1.

——, D. Rosenfeld, A. Pokrovsky, U. Blahak, and A. V. Ryzhkov, 2011: The role of CCN in precipitation and hail in a midlatitude storm as seen in simulations using a spectral (bin) microphysics model in a 2D dynamic frame. *Atmos. Res.*, **99**, 129–146, doi:10.1016/j.atmosres.2010.09.015.

——, T. V. Prabha, N. Benmoshe, G. Pandithurai, and M. Ovchinnikov, 2013: The mechanism of first raindrops formation in deep convective clouds. *J. Geophys. Res. Atmos.*, **118**, 9123–9140, doi:10.1002/jgrd.50641.

Knight, C. A., and N. C. Knight, 1970a: Lobe structures of hailstones. *J. Atmos. Sci.*, **27**, 667–671, doi:10.1175/1520-0469(1970)027<0667:LSOH>2.0.CO;2.

——, and ——, 1970b: The falling behavior of hailstones. *J. Atmos. Sci.*, **27**, 672–681, doi:10.1175/1520-0469(1970)027<0672:TFBOH>2.0.CO;2.

Kumjian, M. R., 2013a: Principles and applications of dual-polarization weather radar. Part I: Description of the polarimetric radar variables. *J. Oper. Meteor.*, **1** (19), 226–242, doi:10.15191/nwajom.2013.0119.

——, 2013b: Principles and applications of dual-polarization weather radar. Part II: Warm- and cold-season applications. *J. Oper. Meteor.*, **1** (20), 243–264, doi:10.15191/nwajom.2013.0120.

——, 2013c: Principles and applications of dual-polarization weather radar. Part III: Artifacts. *J. Oper. Meteor.*, **1** (21), 265–274, doi:10.15191/nwajom.2013.0121.

——, and A. V. Ryzhkov, 2008: Polarimetric signatures in supercell thunderstorms. *J. Appl. Meteor. Climatol.*, **47**, 1940–1961, doi:10.1175/2007JAMC1874.1.

——, S. M. Ganson, and A. V. Ryzhkov, 2012: Freezing of raindrops in deep convective updrafts: A microphysical and polarimetric model. *J. Atmos. Sci.*, **69**, 3471–3490, doi:10.1175/JAS-D-12-067.1.

——, A. P. Khain, N. Benmoshe, E. Ilotoviz, A. V. Ryzhkov, and V. T. J. Phillips, 2014: The anatomy and physics of Z_{DR} columns: Investigating a polarimetric radar signature with a spectral bin microphysical model. *J. Appl. Meteor. Climatol.*, **53**, 1820–1843, doi:10.1175/JAMC-D-13-0354.1.

Lakshmanan, V., and A. Witt, 1997: A fuzzy logic approach to detecting severe updrafts. *AI Appl.*, **11**, 1–12.

——, T. Smith, K. Hondl, G. J. Stumpf, and A. Witt, 2006: A real-time, three-dimensional, rapidly updating, heterogeneous radar merger technique for reflectivity, velocity and derived products. *Wea. Forecasting*, **21**, 802–823, doi:10.1175/WAF942.1.

——, ——, G. J. Stumpf, and K. Hondl, 2007: The Warning Decision Support System–Integrated Information. *Wea. Forecasting*, **22**, 596–612, doi:10.1175/WAF1009.1.

——, K. Hondl, C. K. Potvin, and D. Preignitz, 2013: An improved method for estimating radar echo-top height. *Wea. Forecasting*, **28**, 481–488, doi:10.1175/WAF-D-12-00084.1.

Lemon, L. R., 1998: The radar ''three-body scatter spike'': An operational large-hail signature. *Wea. Forecasting*, **13**, 327–340, doi:10.1175/1520-0434(1998)013<0327:TRTBSS>2.0.CO;2.

Loney, M. L., D. S. Zrnić, J. M. Straka, and A. V. Ryzhkov, 2002: Enhanced polarimetric radar signatures above the melting level in a supercell storm. *J. Appl. Meteor.*, **41**, 1179–1194, doi:10.1175/1520-0450(2002)041<1179:EPRSAT>2.0.CO;2.

Mahale, V. N., G. Zhang, and M. Xue, 2014: Fuzzy logic classification of S-band polarimetric radar echoes to identify three-body scattering and improve data quality. *J. Appl. Meteor. Climatol.*, **53**, 2017–2033, doi:10.1175/JAMC-D-13-0358.1.

Marshall, T. P., D. W. Burgess, G. S. Garfield, J. C. Snyder, R. Smith, D. Speheger, and H. B. Bluestein, 2014: Ground-based damage survey and radar analysis of the El Reno, Oklahoma, tornado. *Proc. 27th Conf. on Severe Local Storms*, Madison, WI, Amer. Meteor. Soc., 13.1. [Available online at https://ams.confex.com/ams/27SLS/webprogram/Paper254342.html.]

Musil, D. J., E. L. May, P. L. Smith Jr., and W. R. Sand, 1976: Structure of an evolving hailstorm, Part IV: Internal structure from penetrating aircraft. *Mon. Wea. Rev.*, **104**, 596–602, doi:10.1175/1520-0493(1976)104<0596:SOAEHP>2.0.CO;2.

NCDC, 2015: *Storm Data.* Vol. 56, No. 6, 922 pp. [Available online at http://www.ncdc.noaa.gov/IPS/sd/sd.html.]

NOAA/NWS/Warning Decision Training Division, 2015: Topic 7: Convective Storm Structure and Evolution. DLOC Course Outline. [Available online at http://www.wdtb.noaa.gov/courses/dloc/outline.php.]

Palmer, R. D., and Coauthors, 2011: Observations of the 10 May 2010 tornado outbreak using OU-PRIME: Potential for new science with high-resolution polarimetric radar. *Bull. Amer. Meteor. Soc.*, **92**, 871–891, doi:10.1175/2011BAMS3125.1.

Park, H., A. V. Ryzhkov, D. S. Zrnić, and K. Kim, 2009: The hydrometeor classification algorithm for the polarimetric WSR-88D: Description and application to an MCS. *Wea. Forecasting*, **24**, 730–748, doi:10.1175/2008WAF2222205.1.

Petersen, W. A., L. D. Carey, K. R. Knupp, C. J. Schultz, and E. V. Johnson, 2008: ARMOR dual-polarimetric radar observations of tornadic debris signatures. Preprints, *24th Conf. on Severe Local Storms*, Savannah, GA, Amer. Meteor. Soc., 3B6. [Available online at https://ams.confex.com/ams/24SLS/techprogram/paper_142043.htm.]

Phillips, V. T. J., A. Pokrovsky, and A. P. Khain, 2007: The influence of time-dependent melting on the dynamics and precipitation production in maritime and continental storm clouds. *J. Atmos. Sci.*, **64**, 338–359, doi:10.1175/JAS3832.1.

——, A. Khain, N. Benmoshe, and E. Ilotoviz, 2014: Theory of time-dependent freezing. Part I: Description of scheme for wet growth of hail. *J. Atmos. Sci.*, **71**, 4527–4557, doi:10.1175/JAS-D-13-0375.1.

——, ——, ——, ——, and A. V. Ryzhkov, 2015: Theory of time-dependent freezing. Part II: Scheme for freezing raindrops and simulations by a cloud model with spectral bin microphysics. *J. Atmos. Sci.*, **72**, 262–286, doi:10.1175/JAS-D-13-0376.1.

Picca, J., and A. V. Ryzhkov, 2012: A dual-wavelength polarimetric analysis of the 16 May 2010 Oklahoma City extreme hailstorm. *Mon. Wea. Rev.*, **140**, 1385–1403, doi:10.1175/MWR-D-11-00112.1.

Pinsky, M., A. P. Khain, and M. Shapiro, 2001: Collision efficiency of drops in a wide range of Reynolds numbers: Effects of pressure on spectrum evolution. *J. Atmos. Sci.*, **58**, 742–764, doi:10.1175/1520-0469(2001)058<0742:CEODIA>2.0.CO;2.

Pruppacher, H. R., and J. D. Klett, 1997: *Microphysics of Clouds and Precipitation.* 2nd ed. Kluwer Academic, 348 pp.

Ryzhkov, A. V., and D. S. Zrnić, 2007: Depolarization in ice crystals and its effect on radar polarimetric measurements. *J. Atmos. Oceanic Technol.*, **24**, 1256–1267, doi:10.1175/JTECH2034.1.

——, T. J. Schuur, D. W. Burgess, and D. S. Zrnić, 2005: Polarimetric tornado detection. *J. Appl. Meteor.*, **44**, 557–570, doi:10.1175/JAM2235.1.

——, M. Pinsky, A. Pokrovsky, and A. Khain, 2011: Polarimetric radar observation operator for a cloud model with spectral microphysics. *J. Appl. Meteor. Climatol.*, **50**, 873–894, doi:10.1175/2010JAMC2363.1.

——, M. R. Kumjian, S. M. Ganson, and A. P. Khain, 2013: Polarimetric radar characteristics of melting hail. Part I: Theoretical simulations using spectral microphysical modeling. *J. Appl. Meteor. Climatol.*, **52**, 2849–2870, doi:10.1175/JAMC-D-13-073.1.

Schultz, C. J., and Coauthors, 2012: Dual-polarimetric radar-based tornado debris signatures and paths associated with tornadoes over northern Alabama during the historic outbreak of 27 April 2011. *Proc. Special Symp. on the Tornado Disasters of 2011*, New Orleans, LA, Amer. Meteor. Soc., J2.2. [Available online at https://ams.confex.com/ams/92Annual/webprogram/Paper200401.html.]

Seliga, T. A., and V. N. Bringi, 1976: Potential use of radar different reflectivity measurements at orthogonal polarizations for measuring precipitation. *J. Appl. Meteor.*, **15**, 69–76, doi:10.1175/1520-0450(1976)015<0069:PUORDR>2.0.CO;2.

Sherman, J. W., 1970: Aperture-antenna analysis. *Radar Handbook*, M. Skolnik, Ed., McGraw-Hill, 9-1–9-40.

Skinner, P., L. J. Wicker, C. K. Potvin, and P. L. Heinselman, 2014: High-resolution ensemble prediction of the 31 May 2013 El Reno, Oklahoma supercell. *Proc. 27th Conf. on Severe Local Storms*, Madison, WI, Amer. Meteor. Soc., 12A.2. [Available online at https://ams.confex.com/ams/27SLS/webprogram/Paper255682.html.]

Smalley, D. J., B. J. Bennett, and M. L. Pawlak, 2003: New products for the NEXRAD ORPG to support FAA critical systems. Preprints, *19th Conf. on Interactive Information and Processing Systems (IIPS) for Meteorology, Oceanography, and Hydrology*, Long Beach, CA, Amer. Meteor. Soc., 14.12. [Available online at https://ams.confex.com/ams/pdfpapers/57174.pdf.]

Smith, P. L., D. J. Musil, A. G. Detwiler, and R. Ramachandran, 1999: Observations of mixed-phase precipitation within a CaPE thunderstorm. *J. Appl. Meteor.*, **38**, 145–155, doi:10.1175/1520-0450(1999)038<0145:OOMPPW>2.0.CO;2.

Snyder, J. C., 2013: Observations and simulations of polarimetric weather radar signatures in supercells. Ph.D. dissertation, University of Oklahoma, 213 pp.

——, and H. B. Bluestein, 2014: Some considerations for the use of high-resolution mobile radar data in tornado intensity determination. *Wea. Forecasting*, **29**, 799–827, doi:10.1175/WAF-D-14-00026.1.

——, and A. V. Ryzhkov, 2015: Automated detection of polarimetric tornadic debris signatures. *J. Appl. Meteor. Climatol.*, **54**, 1861–1870, doi:10.1175/JAMC-D-15-0138.1.

——, H. B. Bluestein, G. Zhang, and S. J. Frasier, 2010: Attenuation correction and hydrometeor classification of high-resolution, X-band, dual-polarized mobile radar measurements in severe convective storms. *J. Atmos. Oceanic Technol.*, **27**, 1979–2001, doi:10.1175/2010JTECHA1356.1.

——, ——, V. Venkatesh, and S. J. Frasier, 2013: Observations of polarimetric signatures in supercells by an X-band mobile Doppler radar. *Mon. Wea. Rev.*, **141**, 3–29, doi:10.1175/MWR-D-12-00068.1.

——, A. V. Ryzhkov, H. B. Bluestein, and S. F. Blair, 2014: Polarimetric analysis of two giant-hail-producing supercells observed by X-band and S-band radars. *Proc. 27th Conf. on Severe Local Storms*, Madison, WI, Amer. Meteor. Soc., 166. [Available online at https://ams.confex.com/ams/27SLS/webprogram/Paper255455.html.]

Straka, J. M., D. S. Zrnić, and A. V. Ryzhkov, 2000: Bulk hydrometeor classification and quantification using polarimetric radar data: Synthesis of relations. *J. Appl. Meteor.*, **39**, 1341–1372, doi:10.1175/1520-0450(2000)039<1341:BHCAQU>2.0.CO;2.

Tanamachi, R. L., H. B. Bluestein, J. B. Houser, S. J. Frasier, and K. M. Hardwick, 2012: Mobile, X-band, polarimetric Doppler radar observations of the 4 May 2007 Greensburg, Kansas, tornadic supercell. *Mon. Wea. Rev.*, **140**, 2103–2125, doi:10.1175/MWR-D-11-00142.1.

——, P. L. Heinselman, and L. J. Wicker, 2015: Impacts of a storm merger on the 24 May 2011 El Reno, Oklahoma, tornadic supercell. *Wea. Forecasting*, **30**, 501–524, doi:10.1175/WAF-D-14-00164.1.

Thompson, R. L., R. Edwards, J. A. Hart, K. L. Elmore, and P. Markowski, 2003: Close proximity soundings within supercell environments obtained from the Rapid Update

Cycle. *Wea. Forecasting*, **18**, 1243–1261, doi:10.1175/1520-0434(2003)018<1243:CPSWSE>2.0.CO;2.

Van Den Broeke, M. S., and S. T. Jauernic, 2014: Spatial and temporal characteristics of polarimetric tornadic debris signatures. *J. Appl. Meteor. Climatol.*, **53**, 2217–2231, doi:10.1175/JAMC-D-14-0094.1.

Wakimoto, R. M., and V. N. Bringi, 1988: Dual-polarization observations of microbursts associated with intense convection: The 20 July storm during the MIST project. *Mon. Wea. Rev.*, **116**, 1521–1539, doi:10.1175/1520-0493(1988)116<1521:DPOOMA>2.0.CO;2.

——, N. T. Atkins, K. M. Butler, H. B. Bluestein, K. Thiem, J. C. Snyder, and J. Houser, 2015: Photogrammetric analysis of the 2013 El Reno tornado combined with mobile X-band polarimetric radar data. *Mon. Wea. Rev.*, **143**, 2657–2683, doi:10.1175/MWR-D-15-0034.1.

Weadon, M., P. Heinselman, D. Forsyth, W. E. Benner, G. S. Torok, and J. Kimpel, 2009: Multifunction phased array radar. *Bull. Amer. Meteor. Soc.*, **90**, 385–389, doi:10.1175/2008BAMS2666.1.

Wilson, J. W., and D. Reum, 1986: "The hail spike": Reflectivity and velocity signature. Preprints, *23rd Conf. on Radar Meteorology*, Snowmass, CO, Amer. Meteor. Soc., 62–65.

——, and ——, 1988: The flare echo: Reflectivity and velocity signature. *J. Atmos. Oceanic Technol.*, **5**, 197–205, doi:10.1175/1520-0426(1988)005<0197:TFERAV>2.0.CO;2.

Wind Science and Engineering Center, 2006: A recommendation for an enhanced Fujita scale (EF-scale). Texas Tech University Wind Science and Engineering Center Rep., 108 pp.

Wurman, J., K. Kosiba, P. Robinson, and T. Marshall, 2014: The role of multiple vortex tornado structure in causing storm researcher fatalities. *Bull. Amer. Meteor. Soc.*, **95**, 31–45, doi:10.1175/BAMS-D-13-00221.1.

Zrnić, D. S., 1987: Three-body scattering produces precipitation signature of special diagnostic value. *Radio Sci.*, **22**, 76–86, doi:10.1029/RS022i001p00076.

——, N. Balakrishnan, C. L. Ziegler, V. N. Bringi, K. Aydin, and T. Matejka, 1993: Polarimetric signatures in the stratiform region of a mesoscale convective system. *J. Appl. Meteor.*, **32**, 678–693, doi:10.1175/1520-0450(1993)032<0678:PSITSR>2.0.CO;2.